Chapter 5

Experimental Apparatus II

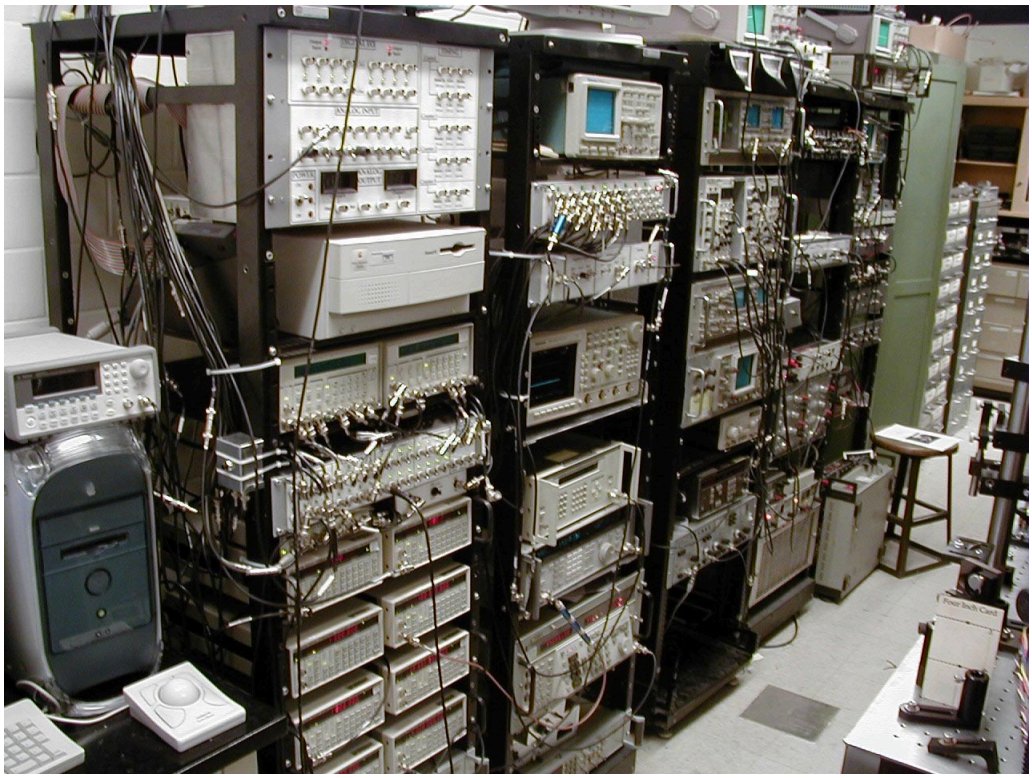

5.1 Overview

In this chapter we discuss several modifications to the experimental apparatus described in Chapter 3. These improvements were necessary to prepare localized atomic wave packets in phase space for the experiments in Chapter 6. The first step towards such localized initial states is further cooling of the atoms beyond what is possible in a typical MOT. We accomplished this additional cooling in a three-dimensional, far-detuned optical lattice, as we discuss in Section 5.2. Further velocity selection well below the recoil limit was accomplished using two-photon, stimulated Raman transitions. We will examine the theory of stimulated Raman transitions as well as their experimental implementation in Section 5.3. It was also necessary to have control over the spatial phase of the optical lattice, so that the wave packet could be shifted to various initial locations in phase space. This spatial control was accomplished through an electro-optic phase modulator placed before the standing-wave retroreflector, as described in Section 5.4. Finally, we trace through the entire state-preparation sequence, using all these atom-optics tools, in Section 5.5, and we discuss the calibration of the optical-lattice potential in the modified setup in Section 5.6.

5.2 Cooling in a Three-Dimensional Optical Lattice

Using the standard techniques of cooling and trapping in a MOT, as described in Chapter 3, we were limited to temperatures on the order of 10 μK for the initial conditions of the experiment. It is desirable, however, to have much lower temperatures for the initial conditions, especially looking towards experiments with minimum-uncertainty wave packets in phase space. Although it has been shown that temperatures below 3 μK can be achieved in cesium using a standard six-beam MOT [Salomon90], our MOT temperatures were substantially higher due to residual magnetic fields from eddy currents in the stainless steel vacuum chamber after the field coils were switched off. One successful approach to achieving additional cooling beyond that of a standard MOT is cooling in a three-dimensional optical lattice. Several methods for cooling in three-dimensional optical lattices have been demonstrated [Kastberg95; Hamann98; Vuletić98; Kerman00], but the method implemented here was based on the setup developed by the group

of David Weiss [Winoto99a; Winoto99b; DePue99; Wolf00; Han01].

The 3D optical lattice was formed by five beams, as illustrated in Fig. 5.1. Three of the beams were in the horizontal plane; two of these beams counterpropagate, and the third is perpendicular to the other two. These beams formed a two-dimensional interference pattern, consisting of a lattice of spots with maximum intensity. This pattern thus forms confining potential wells for red-detuned light, but not for blue-detuned light, where the intensity maxima form scattering barriers for the atoms, resembling the Lorentz gas. The use of three beams for this two-dimensional lattice is important, in that using the minimum number of beams to determine a lattice ensures that the structure of the interference pattern will be stable to phase perturbations [Grynberg93]. In the original implementation of this lattice [Winoto99b; DePue99], four beams (in two counterpropagating pairs) were used to form the horizontal part of the lattice. Because the interference pattern could change its periodicity by a factor of two as the phase of one of the beams varied, the authors in that experiment implemented interferometric stabilization of the beam phases [Han01]. In the realization here, we simply omitted one of the four beams to gain relatively easy stability at the expense of lattice intensity. The omission of one of the

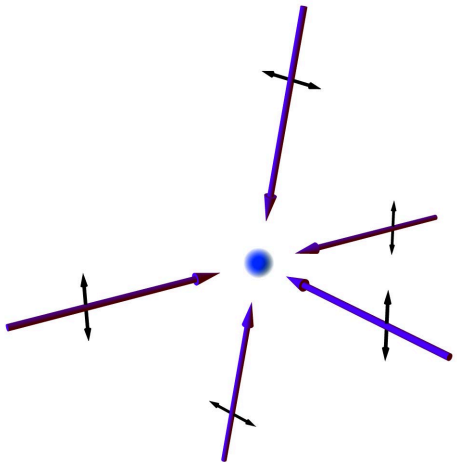

Figure 5.1: Configuration of the beams forming the three-dimensional lattice for additional cooling of the atoms. Five total beams form the lattice, and the directions of the linear polarizations of each beam are indicated. Each of the beams is orthogonal to or counterpropagating with respect to the other beams. The two vertical beams are decoupled from the three horizontal beams by an 80 MHz frequency shift. (Graphics rendered by W. H. Oskay.)

beams was important in allowing long-term storage of the atoms in the lattice, as we describe below, as well as repeatable atomic temperatures.

The other two beams in the 3D lattice counterpropagated in the vertical direction, and they were approximately perpendicular to the three horizontal beams. These beams were offset in frequency by 80 MHz with respect to the horizontal beams. In this arrangement, the interferences with the horizontal lattice oscillate on a time scale that is very fast compared to atomic motion time scales, and thus it is appropriate to regard the vertical beams as decoupled from the horizontal beams in terms of analyzing the interference pattern. Hence, the vertical beams produced a normal 1D standing-wave lattice, which confined the atoms vertically, and the three horizontal beams confined the atoms in the other two dimensions.

Cooling in 3D lattices proceeds by applying the usual MOT beams to the atoms in the lattice. There are several mechanisms by which lattice cooling achieves much lower temperatures than a standard MOT. The first mechanism is that of "adiabatic cooling" [Jessen96], where the application of the lattice acts as an effective refrigerator cycle for cooling the atoms. When the atoms are loaded into the lattice from the initial MOT, they are heated by the increasing potential in order to gain local confinement in the lattice wells. Laser cooling by the MOT beams proceeds as usual, cooling the atoms from the heated temperature back down to normal MOT temperatures. When the lattice is then adiabatically shut off (together with the MOT beams), the temperature is further lowered at the expense of local confinement, in which we are not necessarily interested. An important feature of the lattice configuration implemented here is that because all the light is linearly polarized and far-detuned, the magnetic (Zeeman) sublevels all experience the same energy shift due to the light, and sub-Doppler cooling mechanisms that rely on such degenerate level structure (polarization-gradient cooling [Dalibard89]) proceed as in the free-MOT case. This mechanism was especially important for the setup here, as the atoms could be stored in the lattice until after the magnetic fields decayed, allowing for much better polarization-gradient cooling than we could achieve in the standard MOT. It was also important to extinguish the MOT beams adiabatically, as they likewise produced an optical lattice due to the six-beam interference. The second mechanism for better cooling in the lattice relates

to suppression of the absorption of rescattered light in the MOT. The second-hand absorption of photons that have already been spontaneously scattered by MOT atoms, or "radiation trapping," leads to temperature and density limitations in free-space MOTs [Sesko91; Ellinger94]. These rescattering events are particularly problematic in that they may be much more likely to be absorbed than regular MOT photons, because their cross section for absorption is independent of detuning due to the possibility of taking part in a two-photon stimulated scattering event [Castin98; Wolf00]. In the *festina lente* regime [Castin98], however, where the photon scattering rate (due to lattice photons, as we will mention below) is small compared to the trap oscillation frequency (and thus the vibrational-level splitting), the recoil heating due to these reabsorption events is suppressed [Castin98; Wolf00]. This is because most of the rescattered photons in this regime are scattered elastically in the tight-confinement (Lamb-Dicke) limit, and the probability of an atom changing its vibrational level by scattering such a rescattered photon is small. This suppression of rescatter heating is further enhanced by a third mechanism in lattice cooling, where the cooling proceeds in analogy to a dark MOT [Ketterle93]. This mechanism obtains because the normal repumping light used in the regular MOT is extinguished after the initial cooling phase in the lattice. Most of the atoms are thus in the dark ($F = 3$) hyperfine level, and so the cooling light only affects a small fraction of the atoms at a given time. The far-detuned lattice light provides slow repumping to the trapping transition. Thus, the lifetime for a given vibrational level is set by the scattering rate of optical-lattice light, and not the near-resonant MOT light. Finally, cooling in the lattice has the additional benefit that atoms are separated in individual lattice sites, and thus light-assisted collision losses and other collisional effects are suppressed, resulting in a nearly density-independent cooling rate [Winoto99a].

For the realization here, the light was produced by the same Ti:sapphire laser that provided the 1D time-dependent interaction lattice. An 80 MHz AOM picked off light for the 3D lattice just before the similar pickoff AOM for the 1D lattice light. Another 80 MHz AOM split this beam into two parts, the first order (+80 MHz) having about 1/3 of the light, with the remainder in the unshifted zeroth order. These two beams were spatially filtered by focusing through 50 μm diameter pinholes. The upshifted light formed the vertical lattice beams, while

the unshifted portion was further split in two with a half-wave plate and a polarizing beam-splitter cube to form the horizontal beams. These three beams were all focused onto retroreflecting mirrors on the opposite sides of the chamber so that the beam waist w_0 was 500 μm at their intersection; one of the horizontal, retroreflected beams was blocked to form the five-beam geometry described above. Each of the beams had approximately 90 mW of power. The lattice had a typical detuning of 50 GHz to the red of the $F = 3 \longrightarrow F'$ transition multiplet (or 40 GHz to the red of $F = 4 \longrightarrow F'$), leading to an oscillation frequency in the vertical direction of around 170 kHz (in the harmonic-oscillator approximation) and a scattering rate of around 1 kHz at beam center.

The procedure for lattice cooling began with about 5 s of loading the regular MOT from the background vapor. The optical molasses light intensity was then lowered to 60% of the loading value, and the detuning was increased to 37 MHz (from the 13 MHz used during the loading phase). At the same time, the 3D lattice was turned on adiabatically to minimize the heating of the atoms. The intensity followed the temporal profile $I(t) = I_{\max}(1 - t/\tau)^{-2}$ (for $-800\ \mu\text{s} < t < 0$) [Kastberg95; DePue99], where the time constant τ was 30 μs. During this lattice-loading phase, the anti-Helmholtz fields and repump light were both left on to encourage rapid binding of the atoms to the 3D lattice. After a total of 22 ms in this loading phase, the magnetic fields and repump light were extinguished, and the molasses light was raised back up to 100% intensity. The 3D lattice was maintained at full intensity during the subsequent 298 ms storage time, but the molasses light was ramped linearly down to 77% intensity by the end of this period. This long storage time was sufficient to allow the magnetic fields to decay mostly away (to 70 mG or better, when compensated properly by the Helmholtz coils), although a slowly varying magnetic field was still detectable using the stimulated Raman spectroscopy described below. Then the MOT and 3D lattice beams were ramped down adiabatically according to a similar profile, $I(t) = I_0(1 + t/\tau)^{-2}$ (with the same time constant), over 800 μs. The molasses light began its ramping down about 20 μs before the 3D lattice beams, giving the optimum final temperature.

This lattice-cooling procedure led to an atomic population in the $F = 3$ level with a 1D

temperature (in the horizontal direction) of 400 nK, or $\sigma_p/2\hbar k_{\rm L} = 0.7$. Between 50% and 90% of the atoms remained trapped in the lattice during the cooling cycle, depending sensitively on how well the lattice was aligned. The vertical temperature of 500 nK ($\sigma_p/2\hbar k_{\rm L} = 0.8$) was somewhat higher; the temperature could be made more isotropic by changing the relative beam powers, but at the expense of the horizontal temperature, which was the only important temperature for the experiments here. The lattice worked well over detunings of 25-70 GHz (from $F = 3 \longrightarrow F'$); for closer detunings the final temperature began to rise, and at larger detunings, the fraction retained in the lattice dropped off.

For some experiments, it was necessary to prepare the atoms in the $F = 4$ hyperfine level. This could be conveniently achieved by pulsing on the repumping light for 100 μs after the lattice and molasses fields were extinguished, at the expense of temperature (the final temperature was typically 700 nK after repumping). To implement stimulated Raman velocity selection, as we discuss in the next section, further optical pumping to the $F = 4, m_F = 0$ Zeeman sublevel was necessary, as we discuss in Section 5.3.5.

5.3 Stimulated Raman Velocity Selection

Now we consider the implementation of two-photon, stimulated Raman transitions in cesium for subrecoil (i.e., smaller than the single-photon momentum) velocity selection. After giving a general overview of the theory behind stimulated Raman transitions and velocity selection, we will give the details of our implementation as well as a discussion of optical pumping and internal state selection necessary for a clean velocity-selection method.

5.3.1 Stimulated Raman Transitions: General Theory

We consider the atomic energy level structure shown in Fig. 5.2, where two ground states $|{\rm g}_{1,2}\rangle$ are coupled to a manifold of excited states $|{\rm e}_n\rangle$ by two optical fields. Our goal is to show that under suitable conditions, the atomic population can be driven between the ground states as in a two-level system. We restrict our attention to the case where the fields propagate along a

common axis. In the counterpropagating case, the combined optical field has the form

$$\begin{aligned}\mathbf{E}(x,t) &= \hat{\epsilon}_1 E_{01}\cos(k_1 x - \omega_{\mathrm{L}1}t) + \hat{\epsilon}_2 E_{02}\cos(k_2 x + \omega_{\mathrm{L}2}t) \\ &= \mathbf{E}^{(+)}(x,t) + \mathbf{E}^{(-)}(x,t) \quad ,\end{aligned} \tag{5.1}$$

where $\mathbf{E}^{(\pm)}(x,t)$ are the positive and negative rotating components of the field, given by

$$\mathbf{E}_1^{(\pm)}(x,t) = \frac{1}{2}\left(\hat{\epsilon}_1 E_{01} e^{\pm i k_1 x} e^{\mp i\omega_{\mathrm{L}1}t} + \hat{\epsilon}_2 E_{02} e^{\mp i k_2 x} e^{\mp i\omega_{\mathrm{L}2}t}\right) \quad , \tag{5.2}$$

and $\hat{\epsilon}_{1,2}$ are the unit polarization vectors of the two fields. The results that we will derive also apply to the copropagating case as well upon the substitution $k_2 \to -k_2$.

The free atomic Hamiltonian can then be written

$$H_{\mathrm{A}} = \frac{p^2}{2m} + \hbar\omega_{\mathrm{g}_1}|\mathrm{g}_1\rangle\langle\mathrm{g}_1| + \hbar\omega_{\mathrm{g}_2}|\mathrm{g}_2\rangle\langle\mathrm{g}_2| + \sum_n \hbar\omega_{\mathrm{e}_n}|\mathrm{e}_n\rangle\langle\mathrm{e}_n| \quad , \tag{5.3}$$

and the atom-field interaction Hamiltonian is

$$H_{\mathrm{AF}} = -\mathbf{d}^{(+)}\cdot\mathbf{E}^{(-)} - \mathbf{d}^{(-)}\cdot\mathbf{E}^{(+)} \quad , \tag{5.4}$$

where we have made the rotating-wave approximation, we have assumed that $\omega_{21} := \omega_{\mathrm{g}_2} - \omega_{\mathrm{g}_1} \ll \omega_{\mathrm{eg}_j} := \max\{\omega_{\mathrm{e}_n}\} - \omega_{\mathrm{g}_j}$, and we have in mind that the $|\mathrm{e}_n\rangle$ are nearly degenerate. Additionally,

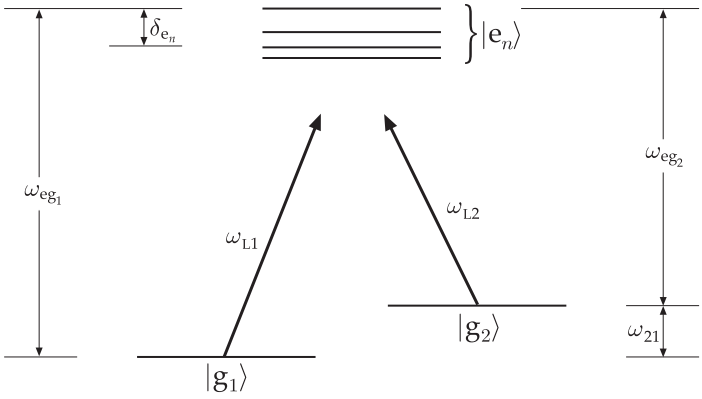

Figure 5.2: Energy level diagram for stimulated Raman transitions. Each ground level $|\mathrm{g}_j\rangle$ is coupled to the excited-state manifold $|\mathrm{e}_n\rangle$ via two laser fields, which are tuned so that their detunings from the excited-state manifold are nearly the same.

we have decomposed the dipole operator $\mathbf{d}$ into its positive- and negative-rotating components,

$$\begin{aligned}\mathbf{d} &= \mathbf{d}^{(+)} + \mathbf{d}^{(-)} \\ &= \sum_n \left(a_{1n}\langle \mathrm{e}_n|\mathbf{d}|\mathrm{g}_1\rangle + a_{2n}\langle \mathrm{e}_n|\mathbf{d}|\mathrm{g}_2\rangle\right) + \sum_n \left(a_{1n}^\dagger\langle \mathrm{e}_n|\mathbf{d}|\mathrm{g}_1\rangle + a_{2n}^\dagger\langle \mathrm{e}_n|\mathbf{d}|\mathrm{g}_2\rangle\right) \quad ,\end{aligned} \tag{5.5}$$

where $a_{jn} := |\mathrm{g}_j\rangle\langle \mathrm{e}_n|$ is an annihilation operator. Substituting (5.5) into (5.4), we find

$$\begin{aligned}H_{\mathrm{AF}} = &-\sum_n \frac{1}{2}\langle \mathrm{e}_n|\hat{\epsilon}_1\cdot\mathbf{d}|\mathrm{g}_1\rangle E_{01}\left(a_{1n}e^{ik_1x}e^{-i\omega_{\mathrm{L}1}t} + a_{1n}^\dagger e^{-ik_1x}e^{i\omega_{\mathrm{L}1}t}\right) \\ &-\sum_n \frac{1}{2}\langle \mathrm{e}_n|\hat{\epsilon}_2\cdot\mathbf{d}|\mathrm{g}_2\rangle E_{02}\left(a_{1n}e^{-ik_2x}e^{-i\omega_{\mathrm{L}2}t} + a_{2n}^\dagger e^{ik_2x}e^{i\omega_{\mathrm{L}2}t}\right) \quad .\end{aligned} \tag{5.6}$$

In writing this expression, we have assumed the detunings $\Delta_{\mathrm{L}j} := \omega_{\mathrm{L}j} - \omega_{\mathrm{eg}_j}$ are nearly equal; hence, to make this problem more tractable, we assume that the field $\mathbf{E}_j$ couples only $|\mathrm{g}_j\rangle$ to the $|\mathrm{e}_n\rangle$. After solving this problem we will treat the cross-couplings as a perturbation to our solutions. If we define the Rabi frequency

$$\Omega_{jkn} := \frac{-\langle \mathrm{e}_n|\hat{\epsilon}_k\cdot\mathbf{d}|\mathrm{g}_j\rangle E_{0k}}{\hbar} \quad , \tag{5.7}$$

which describes strength of the coupling from level $|\mathrm{g}_j\rangle$ through field $\mathbf{E}_k$ to level $|\mathrm{e}_n\rangle$, we arrive at

$$\begin{aligned}H_{\mathrm{AF}} = &\sum_n \frac{\hbar\Omega_{11n}}{2}\left(a_{1n}e^{ik_1x}e^{-i\omega_{\mathrm{L}1}t} + a_{1n}^\dagger e^{-ik_1x}e^{i\omega_{\mathrm{L}1}t}\right) \\ &+\sum_n \frac{\hbar\Omega_{22n}}{2}\left(a_{1n}e^{-ik_2x}e^{-i\omega_{\mathrm{L}2}t} + a_{2n}^\dagger e^{ik_2x}e^{i\omega_{\mathrm{L}2}t}\right)\end{aligned} \tag{5.8}$$

as a slightly more compact form for the interaction Hamiltonian.

Now, before examining the equations of motion, we transform the ground states into the rotating frame of the laser field, as in Chapter 2:

$$\begin{aligned}|\tilde{\mathrm{g}}_j\rangle &:= e^{-i\omega_{\mathrm{L}j}t}|\mathrm{g}_j\rangle \\ \tilde{E}_k^{(\pm)} &:= e^{\pm i\omega_{\mathrm{L}k}t}E_k^{(\pm)} \quad .\end{aligned} \tag{5.9}$$

Also, for concreteness, we will take $\max\{\omega_{\mathrm{e}_n}\} = 0$. Then the rotating-frame, free-atom Hamiltonian is

$$\tilde{H}_{\mathrm{A}} = \frac{p^2}{2m} + \hbar\Delta_{\mathrm{L}1}|\tilde{\mathrm{g}}_1\rangle\langle\tilde{\mathrm{g}}_1| + \hbar\Delta_{\mathrm{L}2}|\tilde{\mathrm{g}}_2\rangle\langle\tilde{\mathrm{g}}_2| + \sum_n \hbar\delta_{\mathrm{e}_n}|\mathrm{e}_n\rangle\langle \mathrm{e}_n| \quad , \tag{5.10}$$

where $\delta_{\mathrm{e}_n} := \omega_{\mathrm{e}_n} - \max\{\omega_{\mathrm{e}_n}\}$ (i.e., $\delta_{\mathrm{e}_n} \leq 0$). The interaction Hamiltonian in the rotating frame is

$$\begin{aligned}\tilde{H}_{\mathrm{AF}} &= -\tilde{\mathbf{d}}^{(+)} \cdot \tilde{\mathbf{E}}^{(-)} - \tilde{\mathbf{d}}^{(-)} \cdot \tilde{\mathbf{E}}^{(+)} \\ &= \sum_n \frac{\hbar\Omega_{11n}}{2}\left(\tilde{a}_{1n}e^{ik_1x} + \tilde{a}_{1n}^\dagger e^{-ik_1x}\right) + \sum_n \frac{\hbar\Omega_{22n}}{2}\left(\tilde{a}_{1n}e^{-ik_2x} + \tilde{a}_{2n}^\dagger e^{ik_2x}\right) \ ,\end{aligned} \tag{5.11}$$

where the annihilation operator $\tilde{a}_{jn}$ is defined in the same way as a_{jn}, but with $|\mathrm{g}_j\rangle$ replaced by $|\tilde{\mathrm{g}}_j\rangle$.

Turning to the equations of motion, we will manifestly neglect spontaneous emission, since $\Delta_{\mathrm{L}j} \gg \Gamma$, where Γ is the decay rate of $|\mathrm{e}_n\rangle$, by using a Schrödinger-equation description of the atomic evolution. Then we have

$$i\hbar\partial_t|\psi\rangle = (\tilde{H}_{\mathrm{A}} + \tilde{H}_{\mathrm{AF}})|\psi\rangle \ , \tag{5.12}$$

where the state vector can be factored into external and internal components as

$$|\psi\rangle = |\psi_{\mathrm{g}_1}\rangle|\tilde{\mathrm{g}}_1\rangle + |\psi_{\mathrm{g}_2}\rangle|\tilde{\mathrm{g}}_2\rangle + \sum_n |\psi_{\mathrm{e}_n}\rangle|\mathrm{e}_n\rangle \ . \tag{5.13}$$

Then if $\psi_\alpha(x,t) := \langle x|\psi_\alpha\rangle$, we obtain the equations of motion

$$\begin{aligned}i\hbar\partial_t\psi_{\mathrm{e}_n} &= \frac{p^2}{2m}\psi_{\mathrm{e}_n} + \frac{\hbar\Omega_{11n}}{2}e^{-ik_1x}\psi_{\mathrm{g}_1} + \frac{\hbar\Omega_{22n}}{2}e^{ik_2x}\psi_{\mathrm{g}_2} + \hbar(\delta_{\mathrm{e}_n} - \Delta_{\mathrm{L}})\psi_{\mathrm{e}_n} \\ i\hbar\partial_t\psi_{\mathrm{g}_1} &= \frac{p^2}{2m}\psi_{\mathrm{g}_1} + \sum_n \frac{\hbar\Omega_{11n}}{2}e^{ik_1x}\psi_{\mathrm{e}_n} + \hbar(\Delta_{\mathrm{L}1} - \Delta_{\mathrm{L}})\psi_{\mathrm{g}_1} \\ i\hbar\partial_t\psi_{\mathrm{g}_2} &= \frac{p^2}{2m}\psi_{\mathrm{g}_2} + \sum_n \frac{\hbar\Omega_{22n}}{2}e^{-ik_2x}\psi_{\mathrm{e}_n} + \hbar(\Delta_{\mathrm{L}2} - \Delta_{\mathrm{L}})\psi_{\mathrm{g}_2} \ ,\end{aligned} \tag{5.14}$$

where we have boosted all energies by $-\hbar\Delta_{\mathrm{L}}$, with $\Delta_{\mathrm{L}} := (\Delta_{\mathrm{L}1} + \Delta_{\mathrm{L}2})/2$ (i.e., we applied an overall phase of $e^{i\Delta_{\mathrm{L}}t}$ to the state vector). Since we assume that $|\delta_{\mathrm{e}_n}| \ll |\Delta_{\mathrm{L}}|$ and $|\Delta_{\mathrm{L}2} - \Delta_{\mathrm{L}1}| \ll |\Delta_{\mathrm{L}}|$, it is clear that the ψ_{e_n} carry the fast time dependence at frequencies of order $|\Delta_{\mathrm{L}}| \gg \Gamma$. We are interested in motion on timescales slow compared to $1/\Gamma$, and the fast oscillations are damped by coupling to the vacuum on timescales of $1/\Gamma$, so we can adiabatically eliminate the ψ_{e_n} by making the approximation that they damp to equilibrium instantaneously ($\partial_t\psi_{\mathrm{e}_n} = 0$). Also, we use $p^2/2m \ll \hbar|\Delta_{\mathrm{L}}|$, with the result,

$$\psi_{\mathrm{e}_n} = \frac{\Omega_{11n}}{2(\Delta_{\mathrm{L}} - \delta_{\mathrm{e}_n})}e^{-ik_1x}\psi_{\mathrm{g}_1} + \frac{\Omega_{22n}}{2(\Delta_{\mathrm{L}} - \delta_{\mathrm{e}_n})}e^{ik_2x}\psi_{\mathrm{g}_2} \ . \tag{5.15}$$

Notice that in deriving this relation, it was important to choose the proper energy shift $-\hbar\Delta_{\mathrm{L}}$ to minimize the natural rotation of the states that remain after the adiabatic elimination; indeed, if the resonance condition that we will derive is satisfied, the two ground states have no natural oscillatory time dependence. This procedure would be much more clear in a density-matrix treatment (as in Section 2.4.1), where the oscillating coherences would be eliminated, but this description is cumbersome due to the number of energy levels in the problem. Using this relation in the remaining equations of motion, we obtain two coupled equations of motion for the ground states,

$$\begin{aligned} i\hbar\partial_t\psi_{\mathrm{g}_1} &= \frac{p^2}{2m}\psi_{\mathrm{g}_1} + \left[\hbar\Delta_{\mathrm{L}1} + \hbar\omega_{\mathrm{AC}1}\right]\psi_{\mathrm{g}_1} + \frac{\hbar\Omega_{\mathrm{R}}}{2}e^{i(k_1+k_2)x}\psi_{\mathrm{g}_2} \\ i\hbar\partial_t\psi_{\mathrm{g}_2} &= \frac{p^2}{2m}\psi_{\mathrm{g}_2} + \left[\hbar\Delta_{\mathrm{L}2} + \hbar\omega_{\mathrm{AC}2}\right]\psi_{\mathrm{g}_2} + \frac{\hbar\Omega_{\mathrm{R}}}{2}e^{-i(k_1+k_2)x}\psi_{\mathrm{g}_1} \quad , \end{aligned} \tag{5.16}$$

where we have removed the energy shift of $-\hbar\Delta_{\mathrm{L}}$. These equations are formally equivalent to the equations of motion for a two level atom, with Rabi frequency

$$\Omega_{\mathrm{R}} := \sum_n \frac{\Omega_{11n}\Omega_{22n}}{2(\Delta_{\mathrm{L}} - \delta_{\mathrm{e}_n})} \tag{5.17}$$

and Stark shifts

$$\omega_{\mathrm{AC}j} := \sum_n \frac{\Omega_{jjn}^2}{4(\Delta_{\mathrm{L}} - \delta_{\mathrm{e}_n})} \quad . \tag{5.18}$$

These equations of motion are just the equations generated by the effective Raman Hamiltonian

$$\begin{aligned} H_{\mathrm{R}} = \frac{p^2}{2m} &+ \hbar(\Delta_{\mathrm{L}1} + \omega_{\mathrm{AC}1})|\tilde{\mathrm{g}}_1\rangle\langle\tilde{\mathrm{g}}_1| + \hbar(\Delta_{\mathrm{L}2} + \omega_{\mathrm{AC}2})|\tilde{\mathrm{g}}_2\rangle\langle\tilde{\mathrm{g}}_2| \\ &+ \hbar\Omega_{\mathrm{R}}\left(a_{\mathrm{R}}e^{i(k_1+k_2)x} + a_{\mathrm{R}}^\dagger e^{-i(k_1+k_2)x}\right) \quad , \end{aligned} \tag{5.19}$$

where the Raman annihilation operator is defined as $a_{\mathrm{R}} := |\mathrm{g}_1\rangle\langle\mathrm{g}_2|$. Noting that the operator $\exp(-ikx)$ is a momentum-shift operator, so that $\exp(-ikx)|p\rangle = |p - \hbar k\rangle$ (and thus $\exp(-ikx)\psi(p) = \psi(p + \hbar k)$, where $\psi(p) := \langle p|\psi\rangle$), it is clear from the form of the effective Raman Hamiltonian that a transition from $|\mathrm{g}_2\rangle$ to $|\mathrm{g}_1\rangle$ is accompanied by a kick to the left of two photon-recoil momenta, and the reverse transition is accompanied by a kick to the right of two photon recoils. We can write out the coupled equations of motion due to the Hamiltonian

(5.19) more explicitly as

$$\begin{aligned} i\hbar\partial_t\psi_{\mathrm{g}_1}(p) &= \left[\frac{p^2}{2m} + \hbar\Delta_{\mathrm{L}1} + \hbar\omega_{\mathrm{AC}1}\right]\psi_{\mathrm{g}_1}(p) + \frac{\hbar\Omega_{\mathrm{R}}}{2}\psi_{\mathrm{g}_2}(p+2\hbar k_{\mathrm{L}}) \\ i\hbar\partial_t\psi_{\mathrm{g}_2}(p+2\hbar k_{\mathrm{L}}) &= \left[\frac{(p+2\hbar k_{\mathrm{L}})^2}{2m} + \hbar\Delta_{\mathrm{L}2} + \hbar\omega_{\mathrm{AC}2}\right]\psi_{\mathrm{g}_2}(p+2\hbar k_{\mathrm{L}}) + \frac{\hbar\Omega_{\mathrm{R}}}{2}\psi_{\mathrm{g}_1}(p) \quad , \end{aligned} \tag{5.20}$$

where $2k_{\mathrm{L}} := k_1 + k_2$. The resonance condition for this transition $|p\rangle|\mathrm{g}_1\rangle \longrightarrow |p+2\hbar k_{\mathrm{L}}\rangle|\mathrm{g}_2\rangle$ is

$$\left[\frac{(p+\hbar k_{\mathrm{L}})^2}{2m\hbar} + \Delta_{\mathrm{L}2} + \omega_{\mathrm{AC}2}\right] - \left[\frac{p^2}{2m\hbar} + \Delta_{\mathrm{L}1} + \omega_{\mathrm{AC}1}\right] = 0 \quad , \tag{5.21}$$

which can be rewritten as

$$4\omega_{\mathrm{r}}\left(\frac{p+\hbar k_{\mathrm{L}}}{\hbar k_{\mathrm{L}}}\right) + (\Delta_{\mathrm{L}2} - \Delta_{\mathrm{L}1}) + (\omega_{\mathrm{AC}2} - \omega_{\mathrm{AC}1}) = 0 \quad . \tag{5.22}$$

Here, we have defined the recoil frequency as before by $\omega_{\mathrm{r}} := \hbar k_{\mathrm{L}}^2/2m = 2\pi \cdot 2.0663$ kHz for the cesium D_2 transition. The first term is just the Doppler shift of the two optical fields due to motion at the average of the upper and lower state momenta. In the copropagating case, this term is typically negligible.

Finally, we account for the effects of the cross-couplings that we previously ignored. The lifetimes of the two ground states are in practice extremely long, so that the line width of the Raman transition is quite narrow, being limited only by the finite interaction time. Since it is assumed that the Raman resonance condition (5.21) is approximately true, the Raman cross-coupling is much further away from resonance than the intended coupling (typically several orders of magnitude in cesium), so this extra Raman coupling can be neglected in a secondary rotating-wave approximation. However, the cross-couplings can induce additional ac Stark shifts of the ground levels. So, we simply modify (5.18) to include these extra shifts:

$$\begin{aligned} \omega_{\mathrm{AC}1} &:= \sum_n \frac{\Omega_{11n}^2}{4(\Delta_{\mathrm{L}} - \delta_{\mathrm{e}_n})} + \sum_n \frac{\Omega_{12n}^2}{4(\Delta_{\mathrm{L}} - \delta_{\mathrm{e}_n} - \omega_{21})} \\ \omega_{\mathrm{AC}2} &:= \sum_n \frac{\Omega_{22n}^2}{4(\Delta_{\mathrm{L}} - \delta_{\mathrm{e}_n})} + \sum_n \frac{\Omega_{21n}^2}{4(\Delta_{\mathrm{L}} - \delta_{\mathrm{e}_n} + \omega_{21})} \quad . \end{aligned} \tag{5.23}$$

These additional Stark shifts may not in general be negligible compared to the original Stark shifts.

We can also obtain an estimate of the spontaneous emission rate by using (5.15) to write the total excited state population in terms of the density matrix elements:

$$\begin{aligned} R_{\rm sc} &= \Gamma \sum_n \rho_{{\rm e}_n{\rm e}_n} \\ &= \sum_n \frac{\Gamma\Omega_{11n}^2}{4(\Delta_{\rm L}-\delta_{{\rm e}_n})^2}\rho_{{\rm g}_1{\rm g}_1} + \sum_n \frac{\Gamma\Omega_{22n}^2}{4(\Delta_{\rm L}-\delta_{{\rm e}_n})^2}\rho_{{\rm g}_2{\rm g}_2} \\ &\quad + \sum_n \frac{\Gamma\Omega_{11n}\Omega_{22n}}{4(\Delta_{\rm L}-\delta_{{\rm e}_n})^2}e^{-i2k_{\rm L}x}\rho_{{\rm g}_1{\rm g}_2} + \sum_n \frac{\Gamma\Omega_{11n}\Omega_{22n}}{4(\Delta_{\rm L}-\delta_{{\rm e}_n})^2}e^{i2k_{\rm L}x}\rho_{{\rm g}_2{\rm g}_1} \quad . \end{aligned} \tag{5.24}$$

Here, $\rho_{\alpha\alpha}$ is the population in state $|\alpha\rangle$, with $\rho_{{\rm g}_1{\rm g}_1} + \rho_{{\rm g}_2{\rm g}_2} \simeq 1$, and this result assumes implicitly that $\Delta_{\rm L1} \approx \Delta_{\rm L2}$. The second two terms represent an enhancement or suppression of spontaneous scattering due to atomic coherences; for example, the state

$$|\psi\rangle = \eta(\Omega_{22n}e^{ik_{\rm L}x}|\psi_{{\rm g}_1}\rangle - \Omega_{11n}e^{-ik_{\rm L}x}|\psi_{{\rm g}_2}\rangle) \tag{5.25}$$

(where η is the appropriate normalization factor) is dark, since $R_{\rm sc}$ vanishes for this state. However, this state is only dark if the cross-couplings can be ignored. More realistically, the scattering rate can be modeled as an incoherent sum over all the couplings of the form $(\Gamma\Omega^2/4\Delta^2)\rho_{{\rm g}_j{\rm g}_j}$, including other fields that are not directly involved in the Raman transition (such as the EOM carrier field, discussed in Section 5.3.3).

5.3.2 Pulse-Shape Considerations

Since the velocity-selective Raman pulses are generally used to "tag" a subset of an atomic distribution according to their momentum, it is important to consider the impact of the temporal pulse profile on the tagged distribution. The simplest pulse profile is the square profile, where the light is turned on at a constant intensity for some duration. Assuming that the atoms are all initially in the same internal atomic state, the tagging process is described by the solution of the optical Bloch equations for the excited state population of a two-level atom with Rabi frequency $\Omega_{\rm R}$, Raman detuning $\Delta_{\rm R}$ (given by the left-hand side of Eq. (5.22)), and with all initial population in the ground Raman state:

$$\rho_{\rm ee}(t) = \frac{\Omega_{\rm R}^2}{\Omega_{\rm R}^2+\Delta_{\rm R}^2}\sin^2\left(\frac{1}{2}\sqrt{(\Omega_{\rm R}^2+\Delta_{\rm R}^2)}\,t\right) \quad . \tag{5.26}$$

From Eq. (5.22), we see that a detuning of $\Delta_{\mathrm{R}} = 4\omega_{\mathrm{r}}$ corresponds to a momentum shift of $\hbar k_{\mathrm{L}}$. This lineshape has wings that decay relatively slowly, with a series of locations where the lineshape goes to zero. The locations of the zeros for an interaction time of δt is given by

$$\Delta_{\mathrm{R}} = \sqrt{\frac{4n^2\pi^2}{(\delta t)^2} - \Omega_{\mathrm{R}}^2} \tag{5.27}$$

for positive integer n. This relation simplifies for specific interaction times; for example, for a "π-pulse" of duration $\delta t = \pi/\Omega_{\mathrm{R}}$, the locations are at $\Delta_{\mathrm{R}} = \Omega_{\mathrm{R}}\sqrt{4n^2-1}$, and for a $\pi/2$-pulse of duration $\delta t = \pi/(2\Omega_{\mathrm{R}})$, the locations are $\Delta_{\mathrm{R}} = \Omega_{\mathrm{R}}\sqrt{16n^2-1}$. These zeros were important in a previous implementation of Raman cooling [Reichel95; Reichel96], where the first zero of the profile (5.26) was placed at zero momentum to form a dark interval where atoms would accumulate. The square-pulse excitation lineshape is plotted in Fig. 5.3 for a $\pi/2$-pulse, a π-pulse, and a 2π-pulse. Note that for the important case of the π-pulse, the central population lobe is characterized by a half width at half maximum of $0.799 \cdot \Omega$.

It is also important to note that because one typically excites a range of detunings with

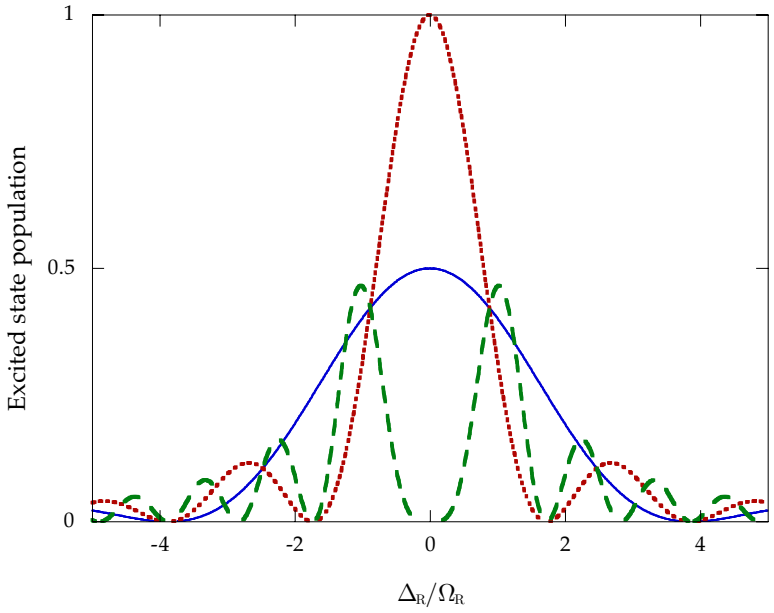

Figure 5.3: Plot of Eq. (5.26), showing excited state population as a function of the detuning from resonance, for three pulse durations: $\pi/2$-pulse, corresponding to an interaction time of $\delta t = \pi/(2\Omega_{\mathrm{R}})$, (solid line); a π-pulse, corresponding to $\delta t = \pi/\Omega_{\mathrm{R}}$ (dotted line); and a 2π-pulse, for $\delta t = 2\pi/\Omega_{\mathrm{R}}$ (dashed line).

a velocity-selective Raman pulse, the transferred population does not undergo simple sinusoidal Rabi oscillations. For a square pulse, the excitation profile (5.26) must be averaged over the atomic velocity distribution. In the limit of a broad velocity distribution, the excited population is proportional to

$$\begin{aligned}\int_{-\infty}^{\infty} \rho_{\mathrm{ee}}(t) d\Delta_{\mathrm{R}} &= \frac{\pi\Omega_{\mathrm{R}}}{2} \mathit{Ji}_0(\Omega_{\mathrm{R}} t) \\ &= \frac{\pi\Omega_{\mathrm{R}}^2 t}{2}\left\{ J_0(\Omega_{\mathrm{R}} t) + \frac{\pi}{2}[J_1(\Omega_{\mathrm{R}} t)\mathbf{H}_0(\Omega_{\mathrm{R}} t) - J_0(\Omega_{\mathrm{R}} t)\mathbf{H}_1(\Omega_{\mathrm{R}} t)]\right\} \quad ,\end{aligned} \tag{5.28}$$

where the $J_n(x)$ are ordinary Bessel functions, the $\mathbf{H}_n(x)$ are Struve functions, and $\mathit{Ji}_n(x) := \int_0^x J_n(x')dx'$. The population in this case still oscillates as a function of time, but with some damping. This function is plotted in Fig. 5.4. Notice that for short times, the function (5.28) reduces to $(\pi/2)\Omega_{\mathrm{R}}^2 t + O(t^2)$, so that one can associate a nonzero transition rate, proportional to Ω_{R}^2 (which is in turn proportional to the product of the laser intensities), as long as $\Omega_{\mathrm{R}} t \ll 1$.

An alternative approach, based on the Blackman pulse profile, was used by the Chu group for Raman cooling [Kasevich92a; Davidson94]. This profile, when normalized to have unit

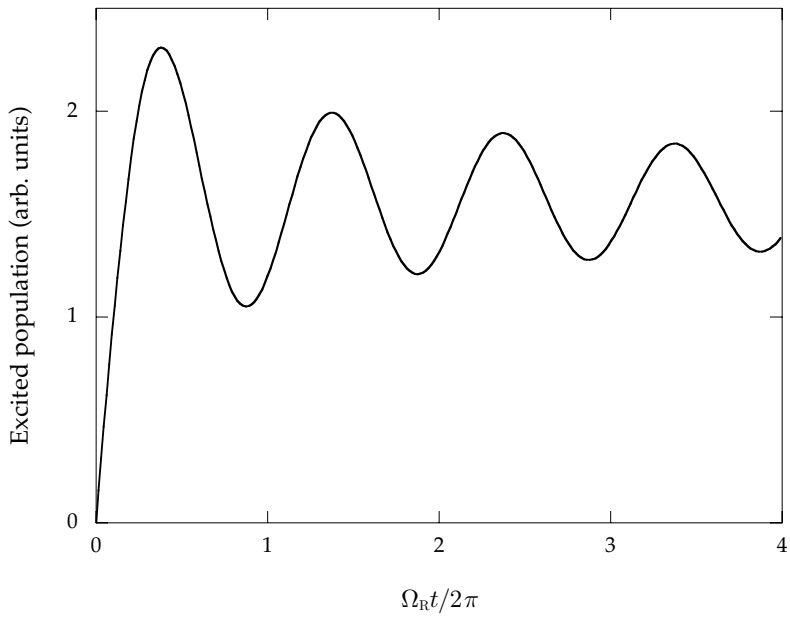

Figure 5.4: Plot of Eq. (5.28), showing excited state population evolution resulting from a square, velocity-selective Raman pulse in a broad atomic velocity distribution. The location of the first minimum is determined by the second zero of $J_0(x)$, which is at $\Omega_{\mathrm{R}} t \approx 0.879 \cdot 2\pi$.

area, can be written as

$$f_{\mathrm{B}}(t) = \frac{1}{0.42\tau}[-0.5\cos(2\pi t/\tau) + 0.08\cos(4\pi t/\tau) + 0.42] \ , \tag{5.29}$$

where τ is the duration (support) of the pulse. The Blackman profile has the property that the tails in the Fourier spectrum are suppressed relative to the square pulse. Hence, the Raman excitation spectrum of the Blackman pulse falls off much more sharply than the corresponding square-pulse spectrum, as shown in Fig. 5.5. However, the implementation of Blackman pulses in a setup where the Raman beams induce an ac Stark shift of the transition is more complicated, since the Raman frequency must be chirped to match the Stark shift in order to get good frequency resolution. (For an 800 μs, square π-pulse, the Raman transition was Stark shifted by around -2 kHz in this setup, which is larger than the 500 Hz effective half-width of the selected momentum group.) Due to the frequency stability issues of the RF electronics discussed below, the experiments in this dissertation used only square Raman pulses.

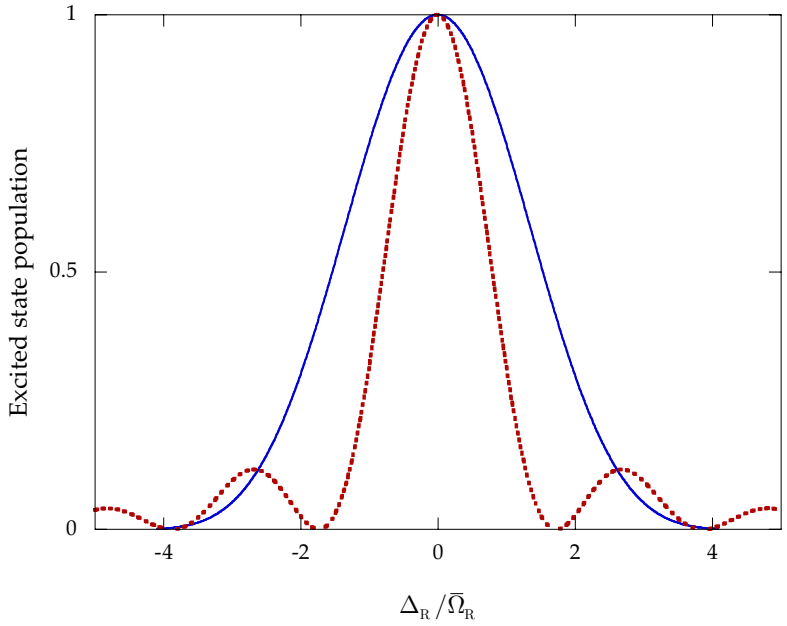

Figure 5.5: Plot of the excitation profile for a Blackman pulse (solid line) and for a square pulse (dotted line). Both pulses are π-pulses and have the same total temporal duration (and hence the same average Rabi frequency $\bar{\Omega}_{\mathrm{R}}$).

5.3.3 Implementation of Stimulated Raman Transitions

The basic hardware setup for implementing stimulated Raman transitions is shown in Fig. 5.6. The Ti:sapphire laser that provided the light for the 1D and 3D optical lattices also provided the light to drive the Raman transitions. A 40 MHz AOM, placed after the two AOMs for the optical lattices and before the wave meter and Fabry-Perot cavity, was used to to pick off the Raman light from the main Ti:sapphire beam line.

The method used to generate the two laser frequencies to drive cesium Raman transitions is similar to the implementation in [Kasevich92b]. The first-order beam from the Raman AOM was split into two components by a 50% beam splitter (or more precisely, a half-wave plate with a polarizing beam-splitter cube). One of the split beams was sent through a New Focus model 4851, 9.28 GHz electro-optic phase modulator (EOM), which put sidebands at ±9.28 GHz on the beam. The driving signal was derived from the 10 MHz output of a highly

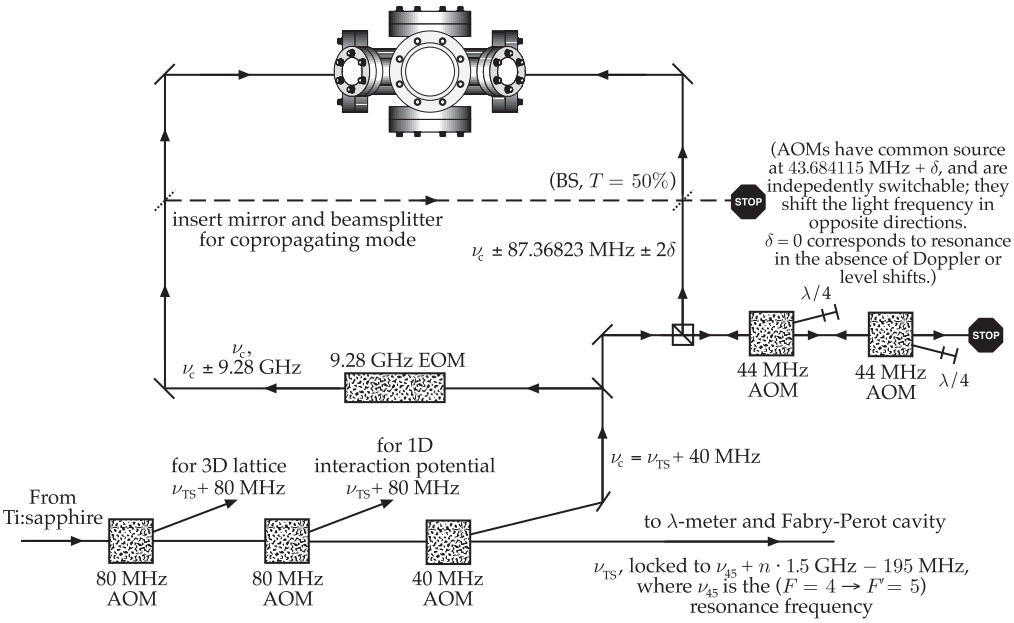

Figure 5.6: Optical layout for implementing stimulated Raman transitions with a high-frequency electro-optic modulator (EOM). The EOM put 9.28 GHz sidebands on the carrier frequency ν_c, and the counterpropagating beam was shifted up or down in frequency by one of two acousto-optic modulators (AOMs), depending on the desired direction of the photon momentum transfer. An extra mirror and beam splitter could be inserted on kinematic mounts to convert the system to copropagating mode.

stable and accurate EFRATOM LPRO rubidium oscillator, which was quadrupled in frequency and then converted to 9.28 GHz by a Delphi Components, Inc. dielectric resonant oscillator (DRO). The DRO output was amplified by a QuinStar Technology, Inc. model CPA09092535-1 solid state amplifier, which was specified to have 25 dB of gain (with 35 dBm maximum output power) at 9.28 GHz. The amplifier output was protected by a Sierra Microwave Technology model SMC-8010 microwave circulator, so that any back-reflections would be terminated into a 50 Ω resistive load rather than the amplifier output port. The signal was transferred to the phase modulator through a 1 m long, Times Microwave Systems LMR-400 cable, which has low loss at 9.28 GHz compared to standard semirigid (RG-402) coaxial wire. The EOM converted about 7% of the carrier into each of the sidebands. The beam was then spatially filtered by focusing through a 40 μm pinhole, converted to circular polarization by a zero-order half-wave plate, and sent into the chamber. This (collimated) beam had a waist parameter w_0 of around 2 mm as it entered the chamber.

The other beam propagated through two 44 MHz tunable AOMs. These AOMs were arranged in a double-pass configuration, with one double-passing the $+1$ order and the other using the -1 order. With this arrangement the output beam could be shifted by ± 88 MHz depending on which AOM was switched on, with some tunability. The output of the double-pass configura-

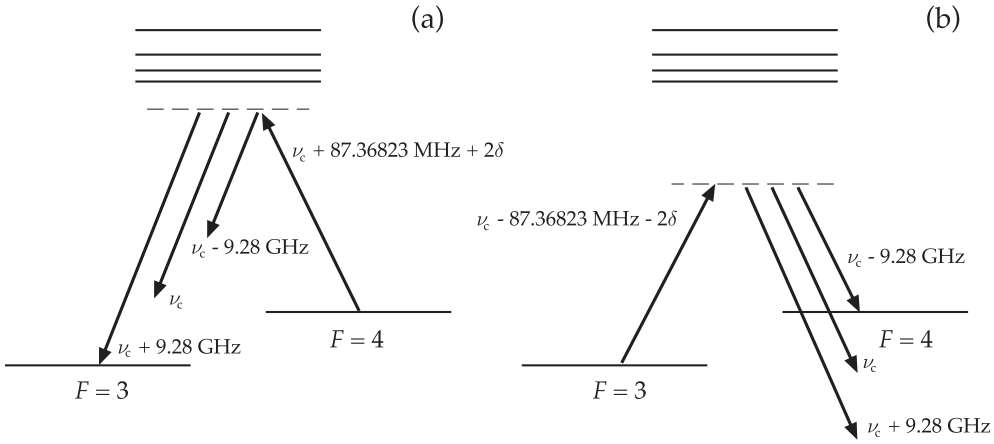

Figure 5.7: Energy-level scheme in cesium for the optical setup in Fig. 5.6. The configuration shown in (a) is for the case when one of the double-passed AOMs shifted the light up by 87 MHz, while case (b) is for the case where the light was shifted down by 87 MHz.

tion was also sent into the vacuum chamber after spatial filtering through a 35 μm pinhole. This beam also had a waist parameter w_0 of around 2 mm in the chamber, and was likewise circularly polarized after passing through a zero-order half-wave plate. The two beams propagated along nearly the same axis as the 1D lattice (with about 1° of horizontal angular separation), to give velocity selectivity in the dimension of interest. The idea behind this arrangement is that the AOM-shifted light and one of the sidebands on the other beam provide the two frequencies to drive the Raman transition. The AOM frequency shift was important to decouple all other pairs of light, so that the other EOM sideband and the EOM carrier had no influence on the atoms besides a Stark shift and some additional spontaneous scattering. The shift was particularly important in decoupling the carrier, which in velocity-selective mode would form a standing wave with the counterpropagating beam. With the frequency shift, this standing wave moved far too quickly ($\sim 10^4$ photon recoils) to have any effect on the atomic motion. Since the ground-state splitting ω_{21} is exactly $2\pi \cdot 9.192\,631\,770$ GHz, driving the AOMs at 43.684 115 MHz (which induces a shift of $\pm$ 87.368 230 MHz) put the Raman transition directly on resonance in the absence of Stark, magnetic, or Doppler shifts.

The tunable RF signal that drove the AOMs needed to be extremely stable, and thus was derived from synthesized signal generators. In the original setup, the signal from a Fluke 6080A/AN synthesizer, operating at 150 MHz, was doubled in frequency by a Mini-Circuits FK-5 doubler. Since the synthesizer had an analog frequency-modulation (FM) input which could change the frequency by up to ± 1 MHz, the doubler effectively increased the "throw" of the synthesizer to ± 2 MHz. The analog FM input was controlled by a Stanford Research Systems DS345 arbitrary waveform synthesizer, connected by a double-shielded coaxial cable to reduce noise contamination on the FM signal. The doubled signal was mixed by a Mini-Circuits ZP-3LH mixer with the output of a WaveTek model 2047 synthesizer, which operated at about 343.7 MHz, to obtain the difference frequency at 43.7 MHz. The mixer output was then amplified by an IntraAction model PA-4 power amplifier and then fed into the appropriate AOM. The synthesizers were both slaved to the Rb oscillator mentioned above for extremely good accuracy and stability, but the analog input of the Fluke unit caused the output frequency to have long-

term drifts (over the course of a day) at the kHz level, which is at the same level as the Fourier width of the Raman selection pulse. Hence, this setup was not suitable for a reliable Raman velocity selection solution, and so the Fluke unit was replaced by a Hewlett-Packard model 8662A synthesizer. The HP unit was much more stable, having drifts at the 100 Hz level over the course of a day, but also had a much smaller FM range of ± 25 kHz. So, the HP unit was more useful for Raman velocity selection, while the Fluke unit was more useful for wide-range sweeps (e.g., while looking for Raman signals initially or beginning to null out magnetic fields). It was also useful to have rapid control of the Raman detuning to chirp the detuning during a pulse, which improved the quality of the spectra in coarse spectral sweeps. For the Raman velocity selection in the state-preparation sequence described below, the FM input on the HP unit was disabled, and the Raman detuning was set by programming the HP unit via the GPIB interface. In this mode, where the FM input was deselected, the RF system had extremely good frequency stability, with a drift at the level of 1 Hz/day.

This configuration allows for two distinct possibilities for driving Raman transitions. When the two beams are counterpropagating, the Raman transitions are velocity-selective, as we argued in the previous section. By choosing which way the double-passed beams are shifted, one also chooses the direction of momentum that the beams impart to the atoms. This idea is illustrated in Fig. 5.7, which shows the optical frequencies in the context of the energy levels of cesium. When the double-passed beam is shifted up in frequency, it drives the $F = 4 \longrightarrow F'$ part of the transition, while the upper sideband on the EOM beam drives the $F = 3 \longrightarrow F'$ part. The lower sideband and the carrier are too far away from resonance to have a significant effect. When the double-passed beam is shifted to the red, however, as in Fig. 5.7(b), the double-passed beam drives the $F = 3 \longrightarrow F'$ part of the Raman transition, while the lower sideband of the EOM beam drives the $F = 4 \longrightarrow F'$ part. The mutual detuning of the Raman beams from resonance is now effectively 9 GHz larger, but the imparted momentum for a given Raman transition is in the opposite direction. For the $F = 3 \longrightarrow F = 4$ Raman transition, the case of Fig. 5.7(a) corresponds to a leftward kick in Fig. 5.6, while the case of Fig. 5.7(b) corresponds to a rightward kick. This dual-AOM arrangement is useful for an implementation of stimulated

Raman cooling, as we discuss briefly below, although for the experiments in this dissertation, we only used one of the AOMs (inducing a positive frequency shift) to drive velocity-selective transitions.

This setup could also be operated in copropagating mode by inserting a mirror to deflect the phase-modulated beam after the spatial filter and inserting a 50% non-polarizing cube beam splitter to combine the two beams with the same polarization. This configuration was useful for nulling the background magnetic fields, as these Raman transitions are much more efficient than in the counterpropagating case (since atoms moving at all velocities can still undergo transitions), and the only energy shifts are Stark and Zeeman shifts. By minimizing the splittings between the resonances due to these copropagating-mode transitions, we could null the background fields to about 10 mG, although we tolerated background fields at the 70 mG level because of long-term drifts in the field-control electronics.

5.3.4 Optical Pushing and Hyperfine State Detection

With this setup, it is possible to drive Raman transitions in cesium, but it is still necessary to have a measurement scheme to detect the internal state populations. Beginning with cooling in the 3D optical lattice, the atoms were cooled in the $F = 3$ ground hyperfine level. As discussed above, a brief repumping pulse transferred the atoms to the $F = 4$ level. At this point we could drive Raman transitions back to the $F = 3$ level. To detect the population transferred by the Raman process, we turned on a beam resonant with the $F = 4 \longrightarrow F' = 5$ cycling transition

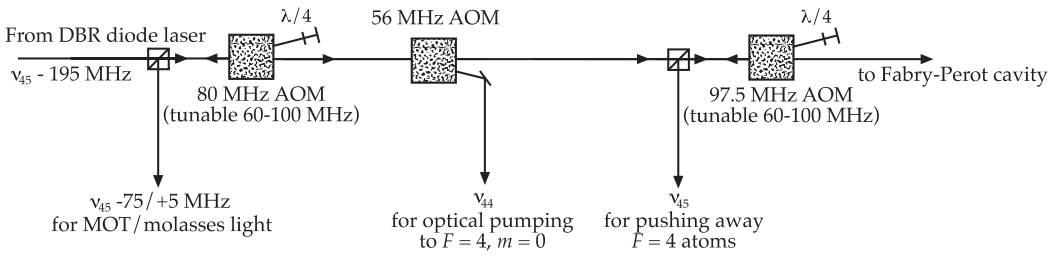

Figure 5.8: Optical layout for other beams needed for Raman tagging. The same laser is used to generate light for the MOT/molasses, the optical pumping into $F = 4, m_F = 0$, and for pushing $F = 4$ atoms out of the interaction region after the tagging.

to accelerate the $F = 4$ atoms to high velocity, leaving only the $F = 3$ atoms in the interaction region; these atoms could then be detected by the usual freezing molasses method or used as a starting point for further atomic manipulation and experimentation. This pushing beam was combined with the phase-modulated Raman beam by a cube beam splitter before the half-wave plate, and thus was circularly polarized as it propagated along the Raman-beam axis. The beam also diverged rapidly (it passed through a 25.4 mm focal length lens about 0.5 m away from the atoms), so that it was large and uniform at the atomic cloud. This light was derived from the DBR laser beam line by a double-passed, 97.5 MHz fixed-frequency AOM, as shown in Fig. 5.8. The light was turned on at low level for 800 μs, accelerating the atoms to over $100 \cdot 2\hbar k_{\mathrm{L}}$. The circular polarization of this beam had the advantage that atoms were optically pumped into the $F = 4, m_{_F} = 4 \longrightarrow F' = 5, m_{_F} = 5$ cycling transition; atoms in this excited state do not decay (by dipole transitions) to the $F = 3$ ground level, and atoms in $F = 4, m_{_F} = 4$ cannot be pumped off-resonantly to the $F' = 4$ excited level (by a dipole transition), so this transition is tightly closed. However, it was still important to use a sufficiently low light level during the first part of the pushing to avoid off-resonant excitation before the atoms were fully optically pumped. This procedure removed the $F = 4$ atoms from the detection region after the drift time with about 99.9% efficiency, with the remaining atoms forming a broad background in the momentum distribution measurements.

To detect the number of atoms transferred by the Raman interaction, we used the usual ballistic-expansion measurement. We ignored the spatial dependence of the CCD image and simply counted the total fluorescence, which after a background subtraction is proportional to the number of atoms in the $F = 3$ level. A sample measurement of Raman Rabi oscillations on resonance (for one of the Zeeman transitions) is shown in Fig. 5.9, which exhibits clean oscillations with a certain amount of damping. For comparison, the Raman Rabi oscillations in the counterpropagating arrangement are shown in Fig. 5.10. The oscillations in this configuration have lower contrast, as we expect from the previous theoretical discussion, and show much lower overall population transfer due to the velocity selectivity. Some detuning-dependent Raman selection profiles for the copropagating mode are shown in Fig. 5.11 for several interaction times.

5.3.5 Hyperfine Magnetic Sublevel Optical Pumping

One difficulty in implementing velocity selection via stimulated Raman transitions in cesium is due to the highly degenerate level structure. For a generic polarization state of the Raman fields, there are 15 possible transitions, each with possibly different Zeeman and Stark shifts, as well as different Rabi frequencies. To make this situation much cleaner, we implemented optical pumping of the atoms into the $F = 4, m_F = 0$ sublevel before driving the Raman transition. We effected this optical pumping using another beam derived from the DBR laser, this time with a 56 MHz AOM (as shown in Fig. 5.10) to shift the beam down in frequency to be on resonance with the $F = 4 \longrightarrow F' = 4$ transition. The beam was spatially filtered and introduced via the MOT beam window on the top of the chamber, so that its linear polarization direction was along the Raman-beam propagation axis. This light was pulsed on for 50 μs, beginning 66 μs before the end of the of the ramp-down time of the 3D optical lattice. Because the $F = 4, m_F = 0 \longrightarrow F' = 4, m'_F = 0$ transition is forbidden in the dipole approximation, the

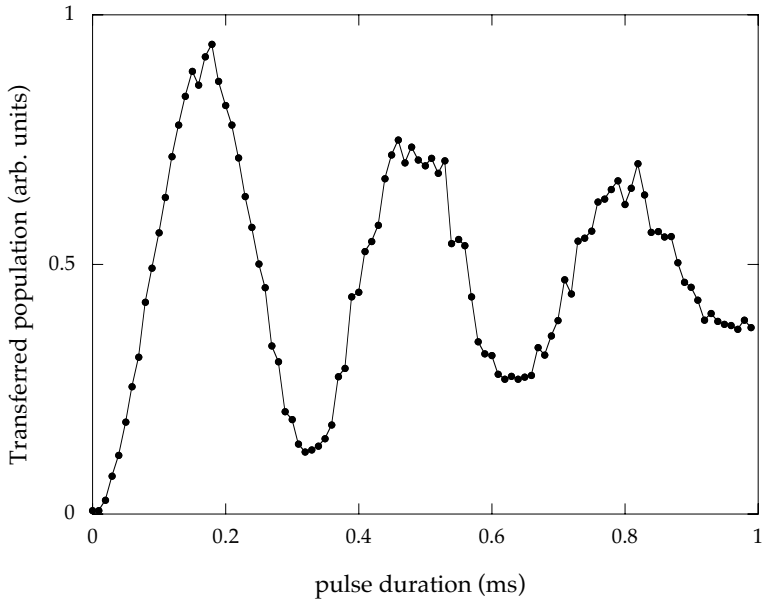

Figure 5.9: Example of an experimental measurement of excited population oscillations for a resonant, stimulated Raman transition in copropagating mode. The damping here is due mostly to spontaneous scattering of the Raman light. The data points here were not averaged over multiple measurements.

atoms accumulated in the $F = 4, m_F = 0$ sublevel after several fluorescence cycles. Atoms that decayed to the $F = 3$ ground level were returned to $F = 4$ by the usual repumping light, which was turned on at the same time as the optical-pumping light. The repumping light was left on until the end of the 3D lattice ramp-down time to ensure that all atoms were in the $F = 4$ ground level. Two of the Helmholtz coils were also pulsed on to provide a 1.5 G bias field along the polarization direction of the pumping light, which swamped other residual magnetic fields and thus prevented remixing of the magnetic sublevels. The coils were turned on 200 μs before the pumping light to allow transients to decay away. This procedure pumped most (>95%) of the atoms into the proper magnetic sublevel. Because the Raman beams were circularly polarized, they drove the atoms from the $F = 4, m_F = 0$ level to the $F = 3, m_F = 0$ level via the $F' = 3, m_F = 1$ and $F' = 4, m_F = 1$ excited states. The atoms thus all experienced the same Raman Rabi frequency, and the Raman transition frequency was insensitive to magnetic fields to first order (this transition is the cesium clock transition that currently defines the measurement

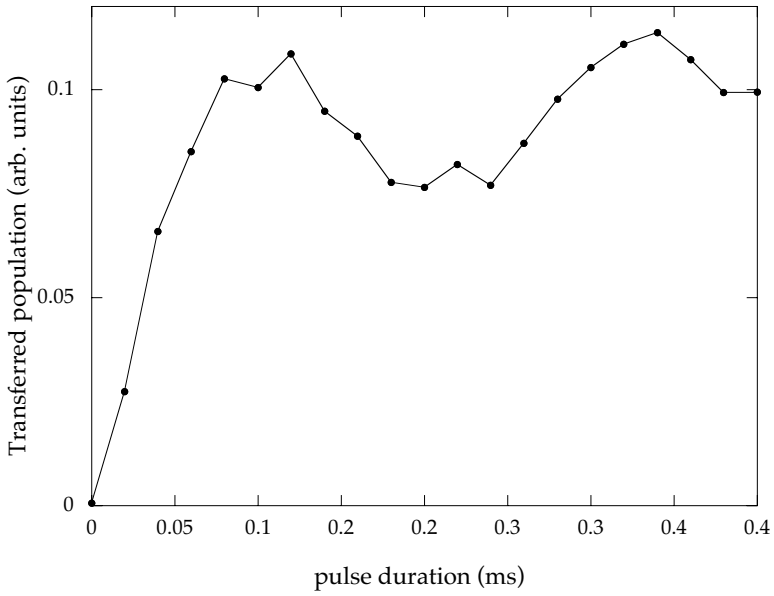

Figure 5.10: Example of an experimental measurement of excited population oscillations for a resonant, stimulated Raman transition in counterpropagating mode. The scale of the vertical axis is the same as in Fig. 5.9. The population transfer is much less efficient due to the velocity selectivity of the counterpropagating configuration. The oscillations also show an upwards trend due to relaxation of nonresonantly coupled atoms. The data points here were not averaged over multiple measurements.

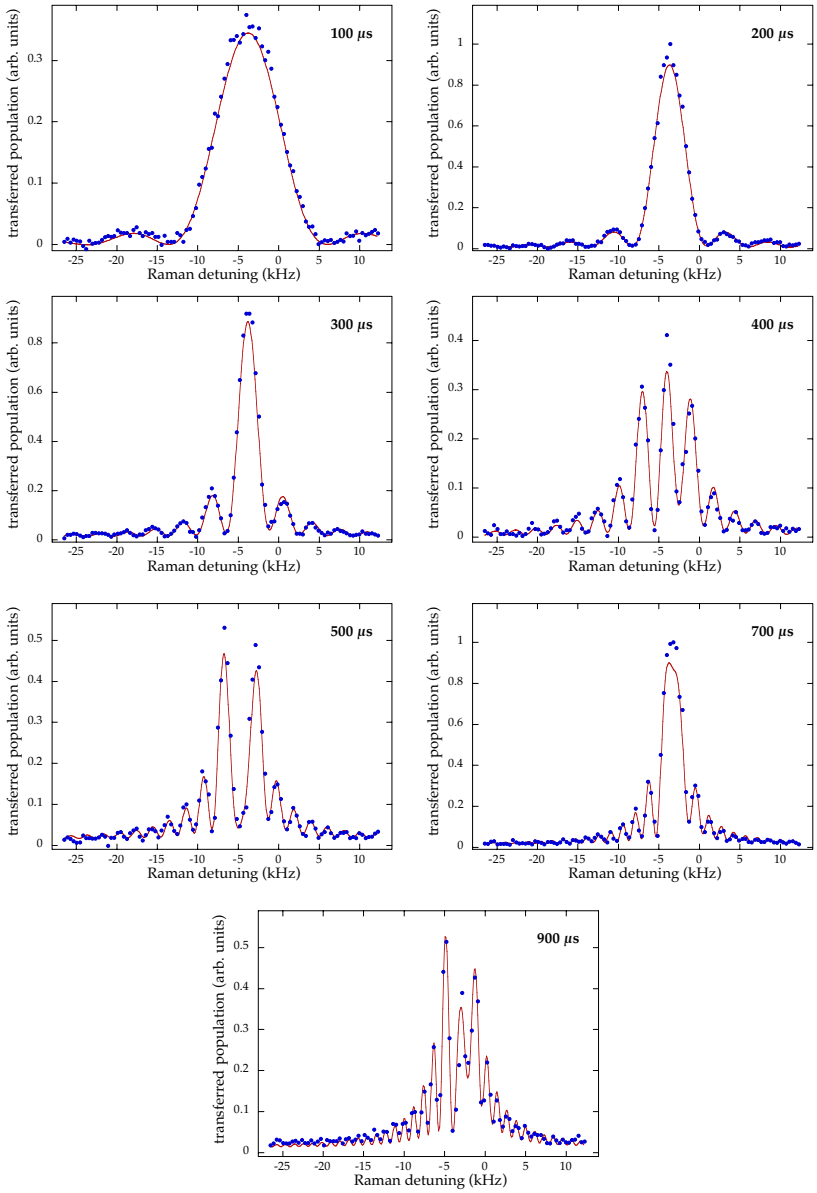

Figure 5.11: Experimental measurement of excited population vs. Raman detuning Δ_{R} for different interaction (square) pulse lengths. The data are shown as points, and the solid lines represent the best fit of a model based on direct integration of the Schrödinger equation for the two-level atom. The asymmetries of the profiles, which is not predicted by Eq. (5.26), can largely be explained by broadening due to the intensity variation of the Gaussian profile of the Raman beams over the atomic sample, which is included in the model. The model was fit simultaneously to all the distributions, and the fitted parameter values are: $\Omega_{\mathrm{R}} = 2\pi \cdot 2.1$ kHz, a coherence damping rate of 21 Hz, and a Raman beam waist $w_0 = 2$ mm (assuming a Gaussian MOT spatial profile with width parameter $\sigma_x = 0.15$ mm). The data points here were not averaged over multiple measurements.

of time). Because of the Zeeman shift due to the large bias field, any atoms left in other magnetic sublevels did not participate in the Raman transition. Unfortunately, these benefits came at the expense of temperature, which increased to 3 μK (or $\sigma_p/2\hbar k_{\rm L} = 1.9$) after the optical pumping (beginning with atoms cooled in the 3D optical lattice). One possible improvement would be to implement sideband cooling into the $m_F = 0$ sublevel [Taichenachev01], but such a scheme requires a considerable increase in the complexity of the experiment.

5.3.6 Implementation of Stimulated Raman Velocity Selection

The 3D lattice cooling, Raman-field setup, pushing-beam setup, and optical-pumping procedure were all important for implementing velocity selection by stimulated Raman transitions. Typically, we selected atoms to be near $p = 0$ as a starting point for further quantum state preparation techniques. The procedure for Raman velocity selection (or "Raman tagging") atoms near $p = 0$ was as follows:

1. Trap and cool atoms in the MOT, and then further cool the atoms in the 3D lattice.

2. Turn on the magnetic bias field along the direction of the Raman beams to define the quantization axis.

3. Use the optical pumping light (during the ramping down of the 3D lattice) to prepare atoms in $F = 4, m_F = 0$ sublevel.

4. Use the Raman beams (both with σ^+ polarization) in counterpropagating mode to tag atoms with $p = 2\hbar k_{\rm L}$ in the $F = 4, m_F = 0$ state to the $F = 3, m_F = 0$ state with $p = 0$. The Raman pulse has appropriate intensity and duration to drive a π-pulse with the desired momentum width.

5. Use the resonant pushing light to remove atoms in $F = 4$.

The atoms were then further manipulated as desired, as described below, and then subjected to the 1D, time-dependent standing-wave interaction as described in the following chapter. In the typical experiment in Chapter 6, the Raman beams drove an 800 μs, square π-pulse. This pulse

should result in a selected profile as in Eq. (5.26), with a half width at half maximum (HWHM) of $0.03 \cdot 2\hbar k_{\mathrm{L}}$. Because of the resolution limit set by the initial size of the MOT cloud, we could not directly verify this profile with our ballistic-expansion measurement, but the expansion rates and the scaling of the fluorescence of the selected atoms with the pulse duration were consistent with the theoretical expectation. This extreme velocity selection was crucial to the success of the experiments in Chapter 6, but had the unfortunate side effect that about 99.5% of the atoms (after 3D lattice cooling) were discarded, causing relatively weak signals in the measurements.

5.3.7 Raman Cooling

With the setup described above, it should in principle be possible to implement Raman cooling, where a large fraction of the atoms could be cooled into a narrow velocity slice as narrow as (or perhaps narrower than) the Raman-tagged slice. Raman cooling works in a repetitive cycle, where atoms at all velocities, except for those in a "target" region near zero momentum, are transferred from the $F = 4$ level to the $F = 3$ level by velocity-selective, stimulated Raman transitions. Then the repumping light is pulsed on to return the atoms to $F = 4$, but with slightly different momentum due to the fluorescence cycle. We implemented the dual-AOM scheme described above so that the direction of the momentum transfer due to the Raman transition could be reversed, and thus during the Raman tagging cycle the atoms on either side of the target region could be moved towards it. However, there are several technical challenges involved in implementing Raman cooling, the most severe of which is the presence of residual magnetic fields. For efficient cooling, the fields must be nulled to 1 mG or better [Reichel94], necessitating the use of a glass chamber (with no ferromagnetic materials) and μ-metal shielding, because the atoms are distributed among the magnetic sublevels. Furthermore, Raman cooling leaves a broad background in the momentum distribution [Reichel94; Reichel95], which must be removed by a final tagging sequence as described above; however, we have noted that transitions associated with different sublevels proceed at different rates, making a clean π-pulse difficult. An optical pumping cycle after cooling would ruin the very cold temperatures, but selecting only atoms in a given sublevel would result in another large hit in atom number.

To circumvent these technical problems, we attempted a modified Raman-cooling procedure, which was performed in the presence of a bias field as above. In addition to the repumping, we also applied the optical pumping light during the recycling stage of each iteration. The target state in this case is the $F = 4, m_F = 0$ state simultaneously with $p = 0$, which is a much more stringent requirement. After a brief attempt, we were not able to cool using this technique, and we instead elected to use averaging as a more straightforward way to address the difficulty of small signals.

5.4 Interaction-Potential Phase Control

An important part of the state-preparation procedure for the experiments in Chapter 6 was the ability to change the phase of the one-dimensional optical lattice. One method for changing the phase is suggested by the analysis in Section 2.6, where we concluded that a frequency difference between the two traveling-wave components results in a moving standing wave. A phase shift can thus be obtained by introducing a pulsed frequency difference. From an experimental point of view, this method is not optimal because it requires splitting the beam, reducing the available intensity (relative to a retroreflecting setup), and it requires careful mode matching of the two traveling waves.

Because the optical lattice was formed by retroreflecting a laser beam in the setup here, the phase of the standing wave was set by the position of the retroreflector. Thus we could move the standing wave simply by moving the retroreflector. We could effectively move the retroreflector by inserting an electro-optic phase modulator (EOM) in the beam path just before the retroreflector. Doing so gave direct electronic control of the optical path length between the atoms and the retroreflector. We used a Conoptics, Inc. model 360-40 EOM, which used a 40 mm long lithium tantalate (LTA) crystal, with a model 302 driver. The EOM had a 2.7 mm clear aperture, and we focused the optical lattice beam onto the retroreflector using a 300 mm focal length lens to ensure that the EOM did not clip the beam. The EOM was also aligned so that the beam propagated slightly off the EOM axis to avoid interference fringes (the reflections of the EOM were also minimized by antireflection coatings on the windows and index-matching

fluid inside the housing). To avoid polarization-modulation effects, it was important to carefully set the EOM angle relative to the lattice-beam polarization. The lattice-beam polarization was set to be horizontal by a cube polarizer mounted just before the entry of the lattice into the chamber. On the other (retroreflecting) side of the chamber, we inserted another cube polarizer before the EOM and adjusted the EOM angle to minimize the signal rejected from the polarizer as the EOM phase was scanned.

In the previous setup of Chapter 3, the stability of the retroreflector was ensured by rigidly mounting it to the vacuum chamber. This new setup was too large to be mounted directly on the chamber, so we constructed a platform to mount the optics, as shown in Fig. 5.12. This platform consisted of a 1/2" thick aluminum plate (jig plate), which rested on a similar piece of 1/2" thick aluminum. A layer of 1/2" thick Sorbothane damping rubber was sandwiched between

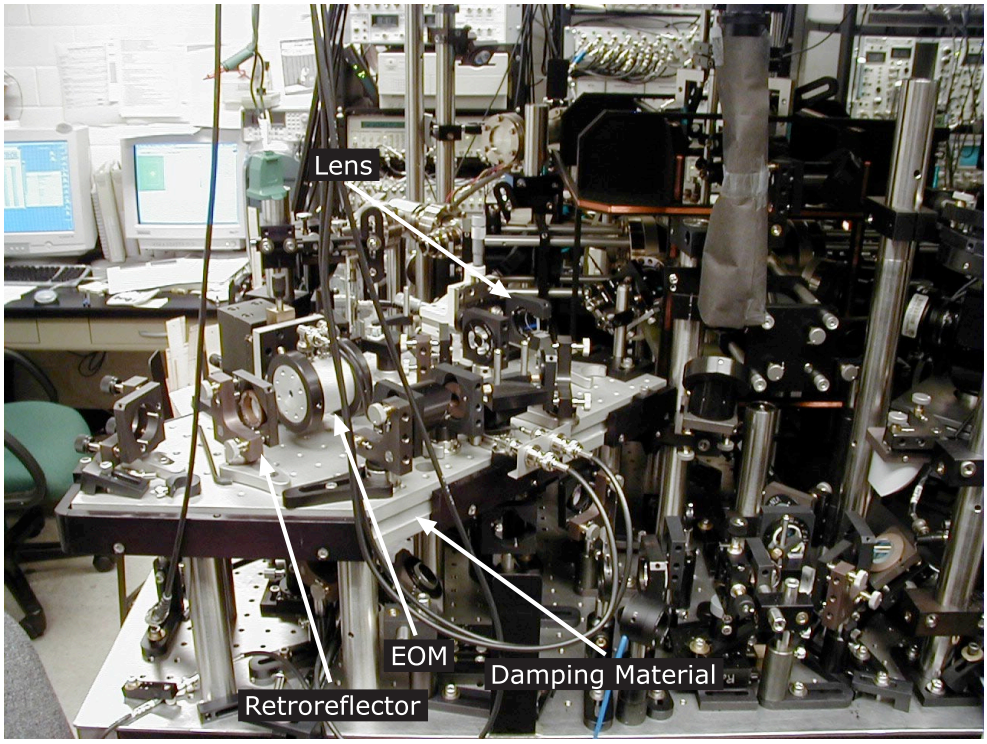

Figure 5.12: Photograph of the phase-control setup for the one-dimensional optical lattice. The components in this setup are shown mounted on the damped, raised, mounting table, and several components for the stimulated Raman optical setup are also visible both on the main and raised tables.

the two aluminum plates. The lower plate was mounted rigidly to the table by six stainless steel posts (1.25" diameter) in an irregular pattern. The optical-lattice beam propagated only 2" above the platform surface to minimize vibrations of the optical mounts. An interferometer constructed on the platform itself measured negligible vibrations, but was incapable of detecting center-of-mass vibrations of the platform, which also contributed to phase jitter of the optical lattice.

This setup provided good phase control over a large range in phase (the EOM controller had an 800 V range, where 250 V corresponds to a 2π phase shift of the lattice phase) on a fast ($\sim$ 1 μs) time scale. One caveat, however, is that fast changes in the phase could excite piezoelectric resonances of the EOM, where the crystal itself begins mechanically ringing as a result of the sudden excitation. This effect is illustrated in Fig. 5.13, where the EOM phase, as measured by a Michelson interferometer, shows ringing in response to a sudden step in the control voltage. The resonance occurred at 150 kHz, with a quality factor Q of about 12. Of the available options from Conoptics, this LTA modulator was the most suitable; the KD*P

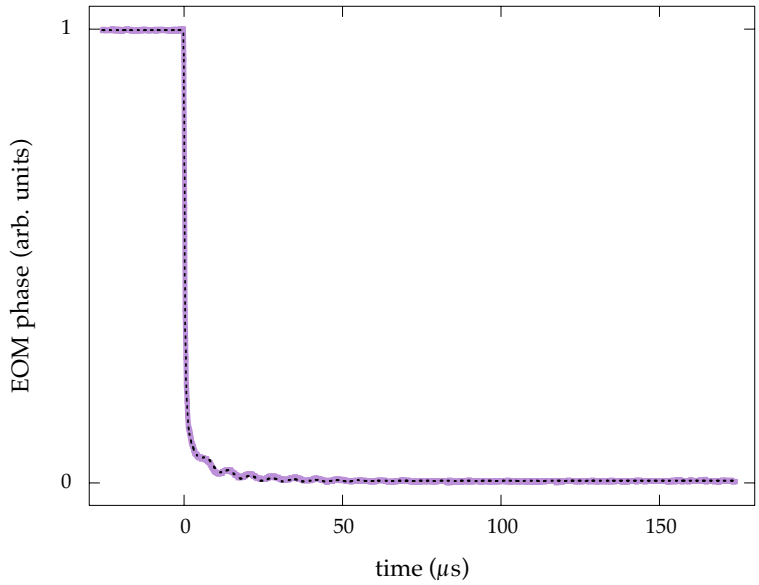

Figure 5.13: Response of the electro-optic modulator to a sudden phase step, as measured interferometrically. The fitted model (dashed line) is a sum of two pure exponentials of different time constants and a damped cosine: $f(t) = 0.87 \cdot \exp(-t/0.37\ \mu\text{s}) + 0.11 \cdot \exp(-t/7.5\ \mu\text{s}) + 0.011 \cdot \cos(2\pi t/6.8\ \mu\text{s} - 0.79) \exp(-t/25\ \mu\text{s}) + 0.004$ (for $t > 0$).

modulators have a smaller available phase range while exhibiting substantially worse ringing than the LTA modulator, even when the crystal is mechanically clamped, and the ADP modulators, which have no piezoelectric resonances, have poor transmission at 852 nm.

5.5 State-Preparation Sequence

Now we will discuss how the various tools presented in this chapter were used to prepare localized initial states in phase space. An overall schematic view of the procedure is illustrated in Fig. 5.14, which shows the condition of the state in phase space at various points in the process. This state-preparation procedure began with the Raman velocity selection process as in Section 5.3.6, which prepared a quantum state that was subrecoil in momentum but delocalized in space. The 1D optical lattice was then turned on adiabatically, with the same temporal profile and time constant (30 μs) as the 3D lattice, although here the leading edge of the profile was clipped 300 μs before the maximum intensity was reached. The lattice caused the atoms to become localized at the potential minima, at the expense of some heating in momentum. Because the initial momentum distribution was narrow compared to the photon recoil momentum $\hbar k_{\mathrm{L}}$, the resulting phase-space distribution had the discrete structure shown in Fig. 5.14. This structure can be understood intuitively in the discrete momentum transfer (in steps of $2\hbar k_{\mathrm{L}}$) from the lattice as it is turned on, and also indicates coherence of the wave packet over multiple potential wells. Recalling from Chapter 2 that for adiabatic processes the band index and quasimomentum are preserved, the atoms were loaded completely into the lowest energy band of the optical lattice. For deep wells (as used in the experiment), the lowest band is approximately the harmonic oscillator ground state (repeated in each well), and thus the overall distribution envelope was approximately a minimum-uncertainty Gaussian wave packet, modulo the standing-wave period. The structure of subrecoil "slices" in the distribution out of an overall Gaussian profile was important in the experiments in Chapter 6, and we will return to this issue in the discussion there.

After the atoms became localized in the lattice potential wells, the phase of the standing wave was shifted by around $1/4$ of the lattice period, which had the effect of displacing the atoms

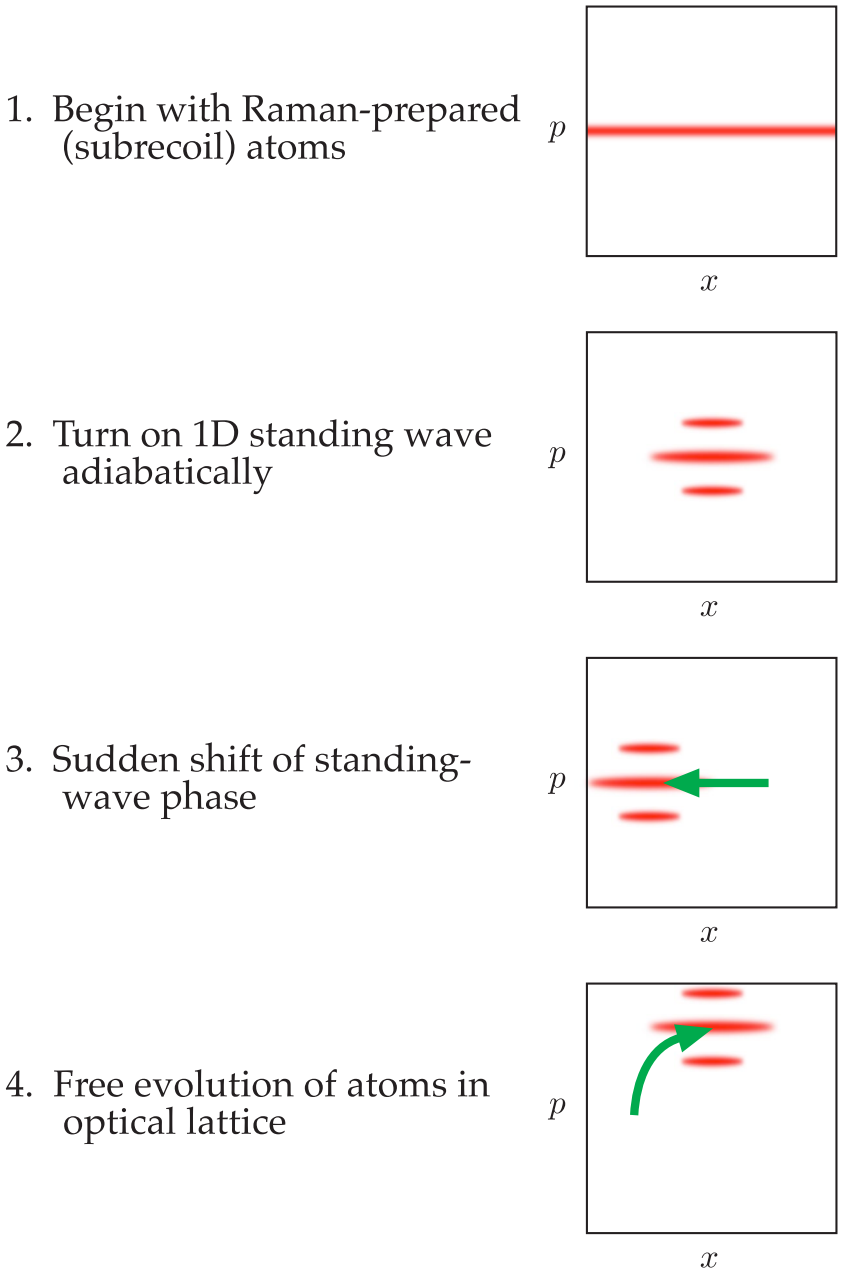

Figure 5.14: Schematic picture of the state-preparation sequence, beginning with the atoms prepared by subrecoil Raman velocity selection. The influence on the atoms in phase space is illustrated. The "striped" character of the distributions is a result of the discrete nature of the momentum transfer to the atoms.

onto the gradients of the potential. They were then allowed to evolve in the stationary optical lattice, where they returned to the potential minima, acquiring momentum in the meantime. In a harmonic potential, this procedure amounts to a boost of the wave packet in momentum, where the distance in momentum is set by the amount of displacement. The anharmonicities in the optical lattice led to a slight distortion of the wave packet, although it was still mostly Gaussian. More importantly, the subrecoil structure of the wave packet was preserved because all of this motional control was induced by the lattice. We refer to this state preparation procedure by the acronym "SPASM," for "State Preparation through Atomic Sliding Motion."

To make this procedure more concrete, the experimental parameters for the first group of data in Chapter 6 (i.e., for $\alpha = 10.5$, $\bar{k} = 2.08$) were as follows: the Raman π-pulse selection time was 800 μs, giving a velocity slice with a HWHM of $0.03 \cdot 2\hbar k_{\mathrm{L}}$; the lattice was turned on to a depth of $\alpha_{\mathrm{p}} = 11.8$ (in the units of Section 2.7); the lattice phase was shifted by 0.25 of the lattice period, and the atoms evolved in the lattice for 6 μs, which was the time after which the atomic momentum was maximized; and the resulting distribution (in momentum) was peaked at $4.1 \cdot 2\hbar k_{\mathrm{L}}$, with a width $\sigma_p = 1.1 \cdot 2\hbar k_{\mathrm{L}}$. For the second group of data ($\bar{k} = 2.08$, for various other values of α), the same Raman velocity selection parameters were used; the optical lattice was turned on to a maximum depth of $\alpha_{\mathrm{p}} = 16.4$; the lattice phase was shifted by 0.21 of the lattice period, and the atoms evolved for 4.5 μs in the lattice; and the prepared distribution was peaked at $4.2 \cdot 2\hbar k_{\mathrm{L}}$, with a width $\sigma_p = 1.7 \cdot 2\hbar k_{\mathrm{L}}$. For the third data group ($\bar{k} = 1.04$), the same Raman velocity selection was again used; the optical lattice was turned on to a maximum depth of $\alpha_{\mathrm{p}} = 30.9$; the lattice phase shift was 0.30 of the standing-wave period, after which the atoms evolved for 3.5 μs; and the momentum distribution was peaked at $8.2 \cdot 2\hbar k_{\mathrm{L}}$, with a width $\sigma_p = 2.1 \cdot 2\hbar k_{\mathrm{L}}$.

The procedure for carrying out the experiments in the following chapter is then very similar to the procedure in Chapter 3, albeit with a much more complicated state-preparation sequence inserted after the initial cooling and trapping of the cesium atoms. After the state-preparation sequence, the atoms were exposed to the temporally modulated optical lattice, where the dynamics of interest occurred. The atoms were then allowed to drift freely in the

dark for 20 ms, and the freezing molasses and CCD camera enabled a measurement of the atomic momentum distribution by imaging the atomic fluorescence for 20 ms.

5.6 Calibration of the Optical Potential

After the introduction of a lens and EOM in the beam path of the 1D optical lattice, we found that the calibration method of Section 3.4.3 no longer produced reliable values for the optical potential depth. This was most likely due to the breakdown of the assumption that the beam waists measured at the knife edge and CCD camera were the same as the waist at the MOT. Thus, the CCD camera was only used to collimate the beam as much as possible: first, the beam was retroreflected with a temporary mirror before the (EOM) lens, and the beam was adjusted so that two beam spots on the CCD (going to and from the vacuum chamber) were approximately the same; then, the temporary mirror was removed, and the longitudinal position of the lens was adjusted to make the spots again equal, thus ensuring that the lens focused the beam onto the retroreflecting mirror.

The state-preparation method outlined above suggests another, *in situ* method to calibrate the potential amplitude. If the Raman velocity selection procedure is used to select a subrecoil momentum sample of the atoms, and the 1D lattice is adiabatically turned on to a large potential depth, an approximately minimum-uncertainty wave packet (modulo the period of the lattice) results, as mentioned above. If the EOM then provides a sudden but small phase shift, the atoms begin to oscillate in the lattice. The oscillation frequency serves as a direct measurement of the potential depth. In the simplest approximation, valid for large potential depths, the oscillations can be regarded as harmonic oscillations near the parabolic potential minima. Recalling from Chapter 2 that the unscaled Hamiltonian for atomic motion in the optical lattice has the form

$$H = \frac{p^2}{2m} - V_0 \cos(2k_{\rm L}x) \ , \tag{5.30}$$

we can expand the potential to $O(x^2)$ about $x = 0$ to obtain the equivalent harmonic oscillator, which has a period

$$T_{\rm HO} = \frac{\pi}{k_{\rm L}}\sqrt{\frac{m}{V_0}} \ . \tag{5.31}$$

However, for a given potential depth V_0, we would actually underestimate the true oscillation period as a result of two effects, anharmonic frequency shifts and quantum effective potential frequency shifts, which we now discuss.

5.6.1 Anharmonicity

Using the same unit scaling as in Chapter 2 (i.e., units where $\hbar = 1$), the pendulum Hamiltonian is

$$H = \frac{p^2}{2} - \alpha_{\rm p} \cos x \quad . \tag{5.32}$$

For a particular value E of the Hamiltonian, we can write the pendulum period as [Tabor89]

$$T(k) = \frac{4}{\sqrt{\alpha_{\rm p}}} F\left(\frac{\pi}{2}, k\right) \quad , \tag{5.33}$$

where $F(\theta, k)$ is the elliptic integral of the first kind, and

$$k = \sqrt{\frac{1}{2}(1 + E/\alpha_{\rm p})} \quad . \tag{5.34}$$

Since $F(\pi/2, 0) = \pi/2$, the small-displacement (harmonic) frequency for this equation is

$$T_{\rm HO} = T(0) = \frac{2\pi}{\sqrt{\alpha_{\rm p}}} \quad , \tag{5.35}$$

so that the fractional period shift due to the lattice anharmonicity is

$$\begin{aligned} \frac{T(k)}{T_{\rm HO}} &= \frac{2}{\pi} F\left(\frac{\pi}{2}, k\right) \\ &= 1 + \frac{k^2}{4} + O(k^4) \quad . \end{aligned} \tag{5.36}$$

Thus, larger amplitudes of oscillation result in longer oscillation periods, which we expect from the fact that the lattice potential drops below the parabolic approximation away from the potential minima.

5.6.2 Quantum Effective Potentials

In addition to the classical anharmonic effects, the oscillation period in the lattice is also increased by the fact that we are considering a quantum wave packet. This effect is illustrated by the numerical simulations in Fig. 5.15. Because of the adiabatic loading of the atoms into the

ground state of the lattice, we can invoke the harmonic approximation to argue that the state within a single well is approximately minimum-uncertainty Gaussian with momentum uncertainty $\sigma_p = (\alpha_\mathrm{p}/4)^{1/4}$ and spatial uncertainty $\sigma_x = (4\alpha_\mathrm{p})^{-1/4}$. From the Ehrenfest equations of motion for the mean values of x and p [Ohanian90],

$$\begin{aligned} \partial_t \langle x \rangle &= \frac{\langle p \rangle}{m} \\ \partial_t \langle p \rangle &= -\langle \partial_x V(x) \rangle \quad , \end{aligned} \tag{5.37}$$

we might expect that the quantum mean values oscillate as in the classical case, but where the potential is "smeared" out by the spatial extent of the wave packet. Performing a convolution of the pendulum potential with the spatial distribution of the Gaussian wave packet, we find that this *effective potential* is still sinusoidal, but with a reduced amplitude:

$$\alpha_\mathrm{eff} = \alpha_\mathrm{p} \exp\left(-\frac{1}{4\sqrt{\alpha_\mathrm{p}}}\right) \quad . \tag{5.38}$$

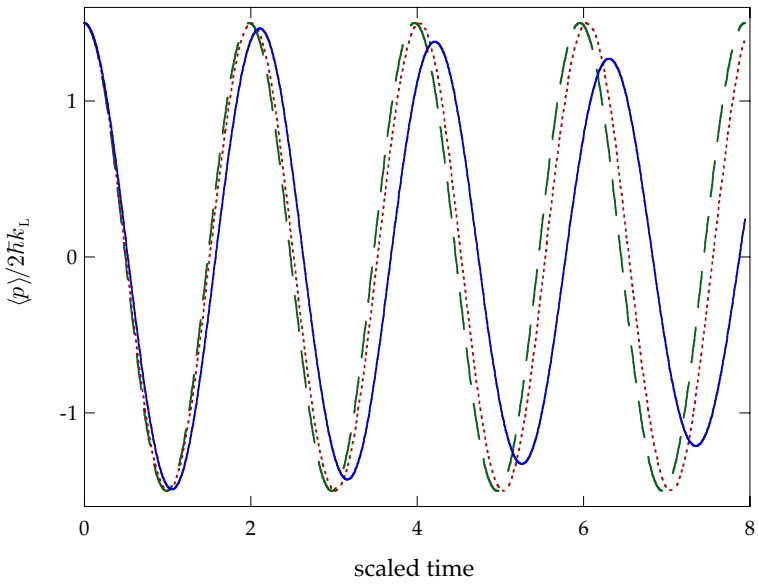

Figure 5.15: Comparison of simulated pendulum oscillations of the classical case in the harmonic approximation (dashed line) to the anharmonic classical pendulum oscillations (dotted line) and the oscillations of an initially minimum-uncertainty quantum wave packet (solid line). The slowing effects of the anharmonicity and quantum wave packet extent are evident here. The system parameters are $\alpha_\mathrm{p} = 10$ (and $\hbar = 1$), with the wave packet and trajectories initially centered at $(x, p) = (0, 1.5)$.

Because we have scaled the units so that $\hbar = 1$, the scaled well depth $\alpha_{\rm p}$ represents the "degree of quantumness" of the pendulum, with larger values representing more classical behavior (and thus a smaller wave-packet area in phase space), as reflected in this quantum scaling factor. Hence, we should expect that the quantum wave packet moves with a longer period due to the reduced effective potential amplitude, and also that the wave packet motion will be further retarded by "classical" anharmonic effects in the effective potential.

5.6.2.1 Wigner-Function Derivation

Hug and Milburn [Hug01] have recently produced a more formal derivation of a quantum scaling factor based on the Wigner-function dynamics, in the context of the amplitude-modulated pendulum. Here we adapt this calculation to the ordinary pendulum, since the derivation does not depend on the temporal modulation of the potential.

We begin with the general equation of motion for the Wigner function (which we introduced in Chapter 1 as the Moyal bracket),

$$\partial_t W(x,p) = -p\partial_x W(x,p) + \frac{i}{\hbar}\left[\sum_{s=0}^{\infty}\frac{1}{s!}\left(\frac{\hbar}{2i}\right)^s \partial_x^s V(x,t)\partial_p^s W(x,p) - \sum_{s=0}^{\infty}\frac{1}{s!}\left(-\frac{\hbar}{2i}\right)^s \partial_x^s V(x,t)\partial_p^s W(x,p)\right] \quad , \tag{5.39}$$

where we will keep the scaled Planck constant $\hbar$ explicit for the time being. We can then insert the pendulum potential,

$$V(x) = -\alpha_{\rm p}\cos(x) \quad , \tag{5.40}$$

with the result

$$\partial_t W = -p\partial_x W + \frac{\alpha_{\rm p}}{\hbar}\sin(x)\sum_{s=0}^{\infty}\frac{1}{s!}\left(\frac{\hbar}{2}\right)^s [1-(-1)^s]\partial_p^s W \quad . \tag{5.41}$$

If make use of the Taylor expansion

$$W\left(x,p+\hbar/2\right) = \sum_{s=0}^{\infty}\frac{1}{s!}[\partial_p^s W(x,p)]\left(\frac{\hbar}{2}\right)^s \quad , \tag{5.42}$$

then Eq. (5.41) becomes

$$\partial_t W(x,p) = -p\partial_x W(x,p) + \frac{\alpha_{\rm p}}{\hbar}\sin(x)\left[W\left(x,p+\hbar/2\right) - W\left(x,p-\hbar/2\right)\right] \quad . \tag{5.43}$$

The goal here to put this equation of motion into "classical form" (of a Liouville equation for a classical phase-space distribution) with an effective potential $V_{\rm eff}$:

$$\partial_t W = -p\partial_x W + \partial_x V_{\rm eff}\partial_p W \quad . \tag{5.44}$$

Hence, we can make the identification

$$\partial_x V_{\rm eff} = \frac{\alpha_{\rm p}}{\hbar}\sin(x)\frac{W\left(x, p+\hbar/2\right) - W\left(x, p-\hbar/2\right)}{\partial_p W(q,p)} \quad . \tag{5.45}$$

We now take the Wigner function to be Gaussian,

$$W(x,p,t) = \frac{1}{\pi\hbar}\exp\left[-\frac{\xi}{\hbar}(x-\langle x\rangle)^2 - \frac{1}{\hbar\xi}(p-\langle p\rangle)^2\right] \quad , \tag{5.46}$$

where $\xi(t)$ is a time-dependent squeezing parameter. So, we can evaluate the terms in the effective potential,

$$\partial_p W(x,p) = -\frac{2(p-\langle p\rangle)}{\hbar\xi}W(x,p) \quad , \tag{5.47}$$

and

$$W(x, p\pm\hbar/2) = \exp\left(-\frac{\hbar}{4\xi}\right)\exp\left[\mp\frac{1}{\xi}(p-\langle p\rangle)\right]W(x,p) \quad , \tag{5.48}$$

and thus the effective potential becomes

$$V_{\rm eff} = -\alpha_{\rm p}\cos(x)\exp\left(-\frac{\hbar}{4\xi}\right)\frac{\sinh\left[\frac{1}{\xi}(p-\langle p\rangle)\right]}{\frac{1}{\xi}(p-\langle p\rangle)} \quad . \tag{5.49}$$

If we assume that the wave packet remains localized (which is implicit in assuming the Gaussian form), then the sinh ratio is approximately unity. Thus, the effective potential is the original potential compressed by a factor of $\exp[-\hbar/(4\xi)]$.

Turning to the quantum pendulum, we can select a preferred value of ξ based on the adiabatic loading into the lattice. Rewriting the Wigner function in terms of σ_x and σ_p and using $\sigma_x\sigma_p = \hbar/2$,

$$\begin{aligned} W(x,p) &= \frac{1}{\sqrt{2\pi\sigma_x}}\exp\left[-\frac{(x-\langle x\rangle)^2}{2\sigma_x^2}\right]\frac{1}{\sqrt{2\pi\sigma_p}}\exp\left[-\frac{(p-\langle p\rangle)^2}{2\sigma_p^2}\right] \\ &= \frac{1}{\pi\hbar}\exp\left[-\frac{-2\sigma_p^2}{\hbar^2}(x-\langle x\rangle)^2 - \frac{1}{2\sigma_p^2}(p-\langle p\rangle)^2\right] \quad , \end{aligned} \tag{5.50}$$

we find that $\xi = 2\sigma_p^2/\hbar = \hbar/(2\sigma_x^2)$. Then, for the quantum pendulum in the harmonic oscillator approximation, we have $\hbar = 1$ and $\sigma_p^2 = \sqrt{\alpha_\mathrm{p}}/2$, so $\xi = \sqrt{\alpha_\mathrm{p}}$. Thus, the effective potential in this case is given by

$$V_{\mathrm{eff}}(x) = -\alpha_\mathrm{p}\cos(x)\exp\left(-\frac{1}{4\sqrt{\alpha_\mathrm{p}}}\right) \quad , \tag{5.51}$$

which is the same result that we found in the simple Ehrenfest (Gaussian convolution) model.

5.6.3 Calibration by Simulation

From the above analysis, we can see that the situation is not entirely simple when deciding what oscillation frequency to expect, given a particular potential depth. To directly account

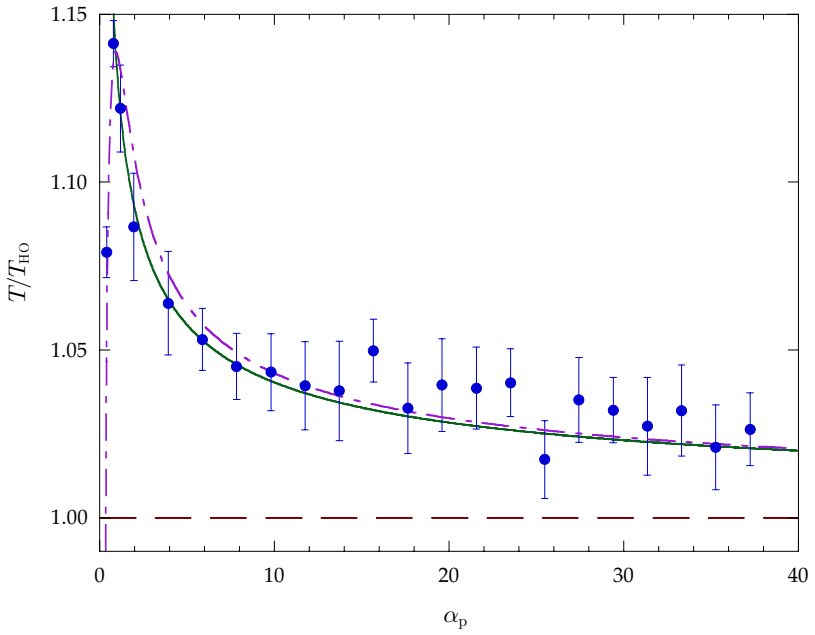

Figure 5.16: Experimentally measured oscillation periods in the optical lattice, normalized to the classical period in the harmonic-oscillator approximation, shown as a dashed line. For comparison the harmonic period in the quantum effective potential is also shown (solid), which agrees reasonably well with the data. Also shown is the splitting of the two lowest eigenstates (with zero quasimomentum) calculated for the sinusoidal potential (dot-dashed line). These latter two curves diverge for small α_p, where the Gaussian approximation for the ground state of the lattice breaks down. The experimental data points are averages over three measurements, and the error bars represent statistical variations among the repeated measurements. The α_p scale was calibrated by comparing the periods in the right half of the plot directly to quantum simulations, as described in the text.

for these effects, we compared the measured wave-packet oscillations to quantum-pendulum simulations. We first extracted the oscillation period of the experimental data, along with the maximum average momentum achieved by the atomic distribution, by fitting an exponentially damped cosine function to the measured $\langle p \rangle$ evolution data. Then a quantum simulation was set up for a minimum-uncertainty wave packet with the same maximum average momentum, and the α_{p} parameter in the simulation was adjusted until the simulated period matched the experimental period. The simulation was facilitated by the fact that the experiment used narrow Raman velocity selection, so that it was a good approximation to use only the discrete plane-wave basis $p = n2\hbar k_{\mathrm{L}}$ (for integer n). Although anharmonic effects were taken into account by using the same maximum momentum in the simulations, these calibrations were typically done with small EOM phase displacements (about 0.05 of the lattice period) to minimize these effects and maintain the Gaussian character of the wave packet as long as possible. When performed with several different lattice intensities, the resulting calibrated values of α_{p} typically agreed at the 3% level or better, although we quote a 5% uncertainty for all the well-depth values in Chapter 6 to account for other systematic effects (such as piezoelectric ringing of the EOM) in the calibration procedure. Fig. 5.16 shows a series of experimentally measured oscillation periods as a function of α_{p}, calibrated as described here.